Journal of Materials Chemistry C

ROYAL SOCIETY OF CHEMISTRY

PAPER

View Article Online
View Journal

Cite this: DOI: 10.1039/d6tc00188b

Tuning structural instability in $Cu_{12-x}Ni_xSb_4S_{13}$ (x = 0, 0.05, 0.2, 0.5) tetrahedrites

Oleksandr Bolielyi,[a] Oleksandr Dobrozhan,[ab] Volodymyr Levytskyi,[a] Alexander A. Tsirlin,[c] Roman Pshenychnyi,[b] Andreas Leithe-Jasper[d] and Roman Gumeniuk*[a]

Received 19th January 2026,
Accepted 1st May 2026

DOI: 10.1039/d6tc00188b

rsc.li/materials-c

$Cu_{12-x}Ni_xSb_4S_{13}$ (x = 0, 0.05, 0.2, 0.5) tetrahedrites were synthesized by the polyol method. Measurements of magnetic susceptibility, specific heat capacity as well as electrical and thermal transport properties indicated a structural phase transition (SPT) of 1st order at T_k = 75–85 K, which is accompanied by strong changes in electronic density of states (EDOS) and entropy for x = 0, 0.05, and 0.2, whereas only weak changes were observed at x = 0.5. However, further temperature-dependent synchrotron high-resolution powder X-ray diffraction (HR PXRD) studies revealed compounds with Ni-content x = 0 and 0.5 to remain body-centered cubic [space group (SG) $I\bar{4}3m$, $a \approx 10.4(1)$ Å] down to 10 K, whereas crystal structures of x = 0.05 and 0.2 became tetragonal (SG $P\bar{4}c2$, $a_{tetr} \approx a_{cub}\sqrt{2}$, $c_{tetr} \approx a_{cub}$) below T_k. Comparing changes of EDOS at the Fermi level [$\Delta N^{(E_F)}$] deduced from magnetic and thermodynamic data with those calculated from density functional theory (DFT) in a rigid-band approximation, we found that $\Delta N^{(E_F)}_{theor} \approx 9$ decreases with Ni content and vanishes for x = 0.5, thus explaining the absence of the tetragonal instability at higher Ni dopings. This study shows that the SPT in tetrahedrites is facilitated by the presence of a minor amount of dopant.

1 Introduction

Waste heat utilization is an important aspect of alternative renewable energy technologies. Thermoelectric (TE) generators (TEGs) are devices allowing the use of temperature gradients across a p–n-junction to obtain a voltage and further generate a direct current (DC). However, TEGs reveal rather poor efficiency ($\approx$5–8%), and their production is associated with high costs and complex manufacturing. The former factor is explained by the dimensionless TE figure-of-merit characterizing efficiency of the members of a p–n-junction. It is given as $ZT = \alpha^2 T\sigma/\kappa$, where α is the Seebeck coefficient, σ is the electrical conductivity and κ is the thermal conductivity. Maximizing ZT requires high σ and low κ, which is difficult to realize in materials because high electronic conductivity goes hand in hand with high thermal conductivity facilitated by the same carriers.[1–4] Therefore, state-of-the-art materials (*e.g.* Bi_2Te_3, PbTe, SiGe, *etc.*) exhibit at best a ZT = 1–2.[5–7] Interestingly, similar TE efficiency has been found in the past decade for some sulfur-containing minerals and their modifications (*e.g.* $Cu_{2-x}S$,[8] $PbS_{0.99}Cl_{0.02}$,[9] Cu_5FeS_4,[10] $Cu_{12}Sb_4S_{13}$,[11] *etc.*). Being available in nature, the latter materials would require lower costs and less preparation effort for TEG production. Besides that, they remain stable upon diverse chemical modifications, which makes their electrical and thermal transport parameters tunable, thus allowing further improvements in TE efficiency. Among the listed minerals, $Cu_{12}Sb_4S_{13}$ tetrahedrite exhibits one of the most remarkable stabilities (*i.e.*, no structural changes) with respect to tuning, and therefore has become an object of numerous studies. Additional impetus to its investigation is given by intriguing physical behaviors such as structural phase transition (SPT) accompanied by a metal-to-semiconductor transition (MST) as well as potential magnetism due to Cu^{2+}-ions.[12,13]

$Cu_{12}Sb_4S_{13}$ was reported for the first time to crystallize with a cubic body-centered structure type [space group (SG) $I\bar{4}3m$, $a \approx 10.3908$ Å, Cu-atoms in 12d and 12e, Sb in 8c, S in 2a and 24g] in ref. 14. Later, it has been shown that the crystallographic positions of one copper and one sulfur are split.[15] Further studies[16,17] revealed tetrahedrites to undergo, in combination with a MST, an SPT at $\approx$88 K, when the structural arrangement becomes tetragonal (SG $P\bar{4}c2$) with parameter a

[a] Institut für Experimentelle Physik, TU Bergakademie Freiberg, Leipziger Straße 23, 09596 Freiberg, Germany. E-mail: roman.gumeniuk@physik.tu-freiberg.de
[b] Department of Electronics and Computer Technology, Sumy State University, 40007 Sumy, Ukraine
[c] Felix-Bloch-Institut für Festkörperphysik, Universität Leipzig, Linnéstraße 5, 04103 Leipzig, Germany
[d] Max-Planck-Institut für Chemische Physik fester Stoffe, Nöthnitzer Straße 40, 01187 Dresden, Germany

enlarged by $\approx \sqrt{2}$. This finding is not confirmed in ref. 15: despite almost the same entropy of SPT, Nasonova *et al.* only observed some perturbations in the cubic structure and no tetragonal distortion.

One of the most important features of the tetrahedrite structural arrangement is its cage-like character. This indicates inhomogeneous bond strength and thus, the appearance of special vibrational properties of loosely bound atoms, known as a 'rattling' effect. The latter strongly affects propagation directions of heat-carrying phonons and results in lowered thermal conductivity, which is beneficial for TE efficiency. Therefore, the 'rattling' effect was extensively investigated by diverse methods, *e.g.* Raman-[18] and neutron- spectroscopies[19] as well as by measurements of specific heat capacity.[20] These studies indicated that Sb lone pair electrons as well as incipient ionic conduction play central roles in the 'rattling' properties of tetrahedrites.

Since further reduction of thermal conductivity in a material can be achieved by implementation of additional structural disorder,[21] numerous attempts at diverse doping (*i.e.*, isoelemental, isoelectronic, *etc.*) of $Cu_{12}Sb_4S_{13}$ have been performed. Some of them are listed here: $Cu_{12-x}Tr_xSb_4S_{13}$ (Tr = Mn,[22] Fe,[23] Co, Zn,[24] Ag,[25] Cd,[26] Hg,[27] *etc.*); $Cu_{12}Sb_{4-x}Pn_xS_{13}$ (Pn = Sn,[28] As[29] *etc.*); and $Cu_{12}Sb_4S_{13-x}Se_x$.[30] Moreover, a number of quinary and senary tetrahedrites are known as well.[12,13] Optimization of different doping types resulted in the achievement of the highest TE efficiencies in $Cu_{11}MnSb_4S_{13}$ (ZT = 1.13 at 575 K)[31] and $Cu_{10.5}Ni_1Zn_{0.5}Sb_4S_{13}$ (ZT = 1.1 at 725 K).[12]

Theoretical calculations within density functional theory (DFT) for ternary as well as doped tetrahedrites have been performed in numerous studies. However, we can cite only some of them within this short introduction, such as recent reports.[24,30,32–38] All of them clearly show pristine $Cu_{12}Sb_4S_{13}$ to be metallic with an enhanced electronic density of states (EDOS) at the Fermi level (E_F). However, since the latter lies near the top of the highest occupied band of the valence band (VB) followed by a broad energy gap of 1.1–1.9 eV, ternary tetrahedrite can be considered as a heavily *p*-doped degenerate indirect semiconductor. Spin-polarized calculations indicate this compound to be non-magnetic. Interestingly, the above-mentioned energy gap is confirmed by direct optical measurements for tetrahedrite thin films[39–42] but to our best knowledge no such reports on bulk or single crystalline samples are currently available.

Ni-doped $Cu_{12-x}Ni_xSb_4S_{13}$ tetrahedrites have attracted significant attention, since their representatives reveal one of the highest TE efficiencies among this class of materials. So, high temperature (300–800 K) electrical and thermal transport properties have been reported for x = 0.5, 1.0, 1.5 and 2.0[43] and x = 0.1–0.4[44] series. $ZT \approx 0.9$ at $\approx$725 K is found for x = 1.0 and 0.2, respectively. Interestingly, temperature dependencies of thermal conductivity and thus ZT are shown to not change gradually with Ni-content x in ref. 44. High ZT = 0.7–0.8 values above 700 K are confirmed for $Cu_{11}NiSb_4S_{13}$[24,45] and $Cu_{10.4}Ni_{1.6}Sb_4S_{13}$.[33,46] However, the latter compound, when synthesized in the form of nanoparticles, reveals ZT = 0.15 at 750 K.[47] Measuring powder neutron diffraction on $Cu_{10.5}Ni_{1.5}Sb_4S_{13}$ as a function of temperature, the authors of ref. 46 evidenced a significant and beneficial role of nickel substitution in both sample purity and stability of the tetrahedrite phase. The $Cu_{11}NiSb_4S_{13}$ nanoparticles are found to balance the loss of stability inherent to nanostructured materials and therefore, make polyol-synthesized doped tetrahedrite indispensable in investigations of TE performance.[48,49] However, despite all intriguing properties, there are almost no reports on low temperature (LT) physical properties of $Cu_{12-x}Ni_xSb_4S_{13}$. Up to now, it is only known that no anomalies related to SPT can be seen in electrical resistivity and Seebeck coefficient down to 2 K for $Cu_{11.5}Ni_{0.5}Sb_4S_{13}$[38] as well as that the effective magnetic moment for $Cu_{11}NiSb_4S_{13}$ deduced from magnetic susceptibility is close to the theoretically calculated one for free Ni^{2+}-ions.[24]

In this work, we present for the first time an extensive LT study including magnetic, thermodynamic, electrical and thermal transport characterization combined with DFT simulations for slightly doped $Cu_{12-x}Ni_xSb_4S_{13}$ (x = 0, 0.05, 0.2, 0.5) tetrahedrites. The performed experiments suggest that a structural phase transition with a clear ordering can only be induced by incorporation of minor amounts of a fourth component in the mentioned crystal structure. We also found that a 'rattling' effect can be detected in the ordered tetragonal structure as well. Different approaches and models used for the interpretation of the obtained results provide new insights into the low temperature crystal chemistry and physics of Ni-doped tetrahedrites.

2 Experimental

To synthesize $Cu_{12-x}Ni_xSb_4S_{13}$ (x = 0, 0.05, 0.2, 0.5) *via* the polyol method, as described in our previous studies,[50–52] copper(II) acetate monohydrate [$Cu(CH_3CO_2)_2{\cdot}H_2O$, Panreac, 98 wt%], nickel(II) acetate tetrahydrate [$Ni(CH_3CO_2)_2{\cdot}4H_2O$, Thermo Scientific Chemicals, 98 wt%], antimony(III) acetate [$Sb(CH_3CO_2)_3$, Thermo Scientific Chemicals, 97 wt%], sulfur [S, Sigma-Aldrich, 99.998 wt%], sodium borohydride [$NaBH_4$, Thermo Scientific Chemicals, 98 wt%], triethylene glycol (TriEG, $C_6H_{14}O_4$, Sigma-Aldrich, 99 wt%), and isopropanol (C_3H_8O, analytical grade) were used. Typically, copper(II) acetate monohydrate (10.00, 9.96, 9.83, 9.58 mmol), nickel(II) acetate tetrahydrate (0.00, 0.04, 0.18, 0.42 mmol), antimony(III) acetate (3.33 mmol), and sulfur powder (10.83 mmol) were mixed with 50 mL of TriEG in a 250 mL three-neck round-bottom flask under an Ar-atmosphere. After magnetic stirring and argon sparging for 20 min, sodium borohydride (2 g dissolved in 25 mL of TriEG) was swiftly injected as a reductant into the reaction mixture. The system was then heated up to T_s = 493 K for 60 min. The final product was self-cooled to 300 K and cleaned thrice *via* centrifugation at 8000 rpm for 5 min, with resuspension in isopropanol. The tetrahedrite powders, obtained with a yield of 90% (1.25 g per batch), were dried at 333 K for 24 h and then annealed at 673 K for 60 min in Ar.

To obtain tetrahedrites with a density of ≈95%, 300 mg of the annealed powder was compacted into pellets (diameter 8.0 mm, thickness 1.5 mm) using a hydraulic press at 35 atm for 60 s. The pellets were then sintered at 673 K for 60 min under an Ar-atmosphere.

Powder X-ray diffraction (PXRD) was carried out on the sintered samples using a Huber G670 Guinier camera ($CuK_{\alpha 1}$ radiation, λ = 1.54056 Å). Temperature dependent high-resolution (HR) PXRD measurements were performed at the ID22 beamline of the European Synchrotron Radiation Facility (ESRF, Grenoble; λ = 0.35460 Å) on powders enclosed in quartz capillaries with the outer diameter of 0.3 mm. The signal was collected by nine scintillation detectors, each preceded by a Si (111) analyzer crystal, in the angle range 2θ = 1–40°. To cool samples down to 10 K, a liquid-helium flow cryostat was used. Phase analysis on the obtained PXRD patterns was performed with the WinXpow software package,[53] whereas Rietveld refinement was carried out by using WinCSD.[54]

Raman spectroscopy (Renishaw inVia Reflex) was used to investigate the crystalline quality and vibrational modes. A red laser (λ = 785 nm) with an output power of I = 0.50 mW was employed at room temperature. Raman spectra were collected for 60 s with five repetitions with a 10× magnification objective and 800 lines per mm grating.

The microstructural analysis of the $Cu_{12-x}Ni_xSb_4S_{13}$ tetrahedrites was performed using scanning electron microscopy (SEM, SEO-SEM Inspect S50-B) equipped with an X-ray detector for energy dispersive analysis (EDX). The measurements were done at an accelerating voltage of 15 kV and a beam current of 10 mA. Elemental mapping confirmed the homogeneous distribution of Cu, Ni, Sb, and S as well as the average grain size of 50 to 200 nm. The obtained chemical compositions are presented in Table S1. They mainly agree well with the nominal ones, with the exception of sulfur-content, which seems to be regularly slightly underestimated. In addition, as a limitation of chemical analysis, EDX is rather weakly sensitive to the extremely low Ni-contents (x = 0.05). An independent, albeit destructive, ICP-chemical analysis of big sample batches could be envisaged.

The field and temperature dependent magnetic susceptibility and specific heat capacity of $Cu_{12-x}Ni_xSb_4S_{13}$ were measured on small pieces with a mass of ≈5 mg using VSM and specific heat options of a DynaCool-12 instrument (Quantum Design). To measure electrical resistivity, Seebeck coefficient and thermal conductivity, bars with dimensions of ≈1 × 1 × 10 mm were cut from the pressed pills and measured using the TTO setup of the same instrument. To estimate charge carrier concentration and their mobility, Hall effect measurements were done on quadratic plates (≈5 × 5 × 1 mm) in the van-der-Pauw geometry.

The electronic band structure and density of states (EDOS) were calculated within the local density approximation (LDA) of density-functional theory (DFT) using the full-potential FPLO code (version 18.00-52.38).[59] The scalar relativistic calculation was performed applying the exchange–correlation potential by Perdew and Wang.[60] The k-mesh included 1728 and 512 points in the first Brillouin zone for cubic and tetragonal idealized structures, respectively.

3 Results and discussion

3.1 Crystal structure

Phase analysis performed on the high-resolution (HR) synchrotron powder X-ray diffraction (PXRD) patterns obtained at 293 K for the $Cu_{12-x}Ni_xSb_4S_{13}$ (x = 0, 0.05, 0.2, 0.5) compounds indicated them to contain only one phase with the cubic tetrahedrite structure type [space group (SG) $I\bar{4}3m$, unit cell parameter (UCP) $a \approx 10.3$ Å].[14] The same observation was made at 100 K and for x = 0 and 0.5 even down to 10 K. However, further refinements of crystal structures applying the tetrahedrite model proposed in ref. 14 resulted in an unphysically large atomic displacement parameter (ADP) for the Cu2-atom occupying the 12e-site [*i.e.*, $B_{iso}(Cu2) \approx 4B_{iso}(Cu1)$]. A similar situation for the ternary $Cu_{12}Sb_4S_{13}$ is reported in ref. 15. To solve the problem, the authors proposed to place Cu2 in the 24g crystallographic position with occupational parameter $G \approx 0.5$. In the following we used this model for our refinements. Their crystallographic parameters, obtained atomic coordinates, ADPs, G-values and interatomic distances are collected in Tables S1 and S3, respectively. A typical refined profile is presented for the HR PXRD pattern of $Cu_{11.95}Ni_{0.05}Sb_4S_{13}$ at 100 K in Fig. 1b. We point out that the residual electronic density in all refinements was $\lesssim 1$ e$^-$ Å^{-3}, which is a clear indication of the absence of any additional occupied atomic positions in the studied compounds.

Substitution of Cu by smaller Ni (r_{Cu} = 1.28 Å, r_{Ni} = 1.25 Å[61]) in the crystal structure of $Cu_{12-x}Ni_xSb_4S_{13}$ is expected to result in a reduction of UCP within this series. However, it is not the case for the compounds studied in this work (Table S1). Seeking to understand the obtained dependence, we analyzed the UCPs for Ni-doped tetrahedrites available in the literature. As one can see from the inset to Fig. 1b, they reveal a strong scattering, which is far beyond the precision of the modern XRD technique. Furthermore, a study[44] suggests a change of lattice volume of ≈5 Å^3 per doping with 0.1Ni-atom. All these could indicate difficulties in determining the true composition of the investigated tetrahedrites, which is additionally hampered by the existence of the intrinsic $Cu_{12\pm y}Sb_4S_{13}$ homogeneity range.[46,62] However, a linear decrease of UCP with increasing Ni-content for $0 \le x \le 2$, which included our data for x = 0 and 0.5, could be clearly confirmed (blue line in inset to Fig. 1b). Deviation from this linearity of UCPs of compounds with low Ni-content (x = 0.05 and 0.2) should be obviously explained by structural phase transitions (SPTs) accompanied by the clear cubic ↔ tetragonal change in the crystal structure, which is not the case for undoped tetrahedrite and those with $x \ge 0.5$. In line with our findings, no SPTs have been reported up to now in analogous transition metal (Tr)-doped tetrahedrites $Cu_{12-x}Tr_xSb_4S_{13}$ (Tr = Mn,[22] Fe,[23] Co, Zn,[24] Ag,[25] Cd,[26] Hg,[27] *etc.*)

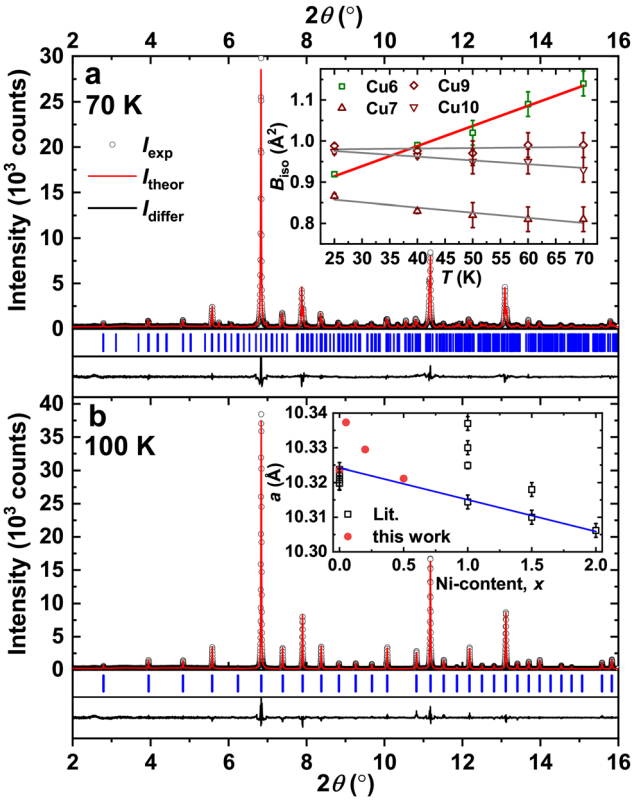

Fig. 1 High resolution powder X-ray diffraction patterns for $Cu_{11.95}Ni_{0.05}Sb_4S_{13}$ at 70 K (a) and 100 K (b). Inset to (a): temperature dependence of thermal displacement parameters of Cu-atoms from the [S2Cu$_6$]-octahedra in the tetragonal $Cu_{11.95}Ni_{0.05}Sb_4S_{13}$ structure. Inset to (b): evolution of UCP with increasing Ni-content x in $Cu_{12-x}Ni_xSb_4S_{13}$. Data from earlier reports are for x = 0,[24,46,55,56] x = 1,[24,49,57] x = 1.5[46,47] and x = 2.[58]

To analyze the influence of Ni-doping on the structural changes in tetrahedrites, we calculated the relative expansion (positive)/contraction (negative) given as $\eta = [(d^{(x)} - d^{(x=0)}/d^{(x=0)}] \times 100\%$ for the bonding interatomic distances (d) as well as UCP at RT (Fig. S1, *cf.* Table S1). Following the decrease in UCP with increasing x, η is negative ($\approx -0.02\%$) while considering the x = 0 and x = 0.5 compositions. It also remains negative for the majority of the contacts with the only exclusions being for Cu1–4S2 ($\approx$+0.2%) and Cu2–2S2 ($\approx$+0.08%). Interestingly, d in the compounds with Ni-content x = 0.05 and x = 0.2 reveals similar trends, but in a more pronounced manner. For instance, the expansions therein for Cu1–4S2 are $\eta \approx$ +0.6% and $\approx$+0.4%, respectively. The exceptions are Cu2–1Sb and Cu2–2S2 contacts, which shrink and elongate, respectively, within x = 0 and x = 0.5 (no structural distortion) and become longer and shorter for x = 0.05 and x = 0.2 (cubic ↔ tetragonal phase transition). Such a complex variation of the interatomic contacts within the $Cu_{12-x}Ni_xSb_4S_{13}$ series obviously indicates the presence of several competing factors (*e.g.* size, electronegativity, *etc.*) that determine the chemical bonding in tetrahedrites. The latter would require a thorough analysis, which is beyond the scope of this study.

As it is stressed above, no symmetry changes are observed for the ternary $Cu_{12}Sb_4S_{13}$: refinements of the PXRD patterns measured at 293 K, 100 K and 10 K indicated cubic symmetry (Tables S1 and S3). This is in contradiction with the earlier reports of the cubic ↔ tetragonal transition for T < 80 K[16,17] and in line with the data from ref. 15. Similarly, as discussed in the latter work, we observe almost the same behavior of some structural parameters characteristic for the phase transition. So, for T < 80 K, it is accompanied by a drastic increase of the ADP of the Cu2-atom [B_{iso}(Cu2)] (Fig. S2a) as well as the Cu2–Sb-distance [$d_{(Cu2-Sb)}$, Fig. S2e], whereas $d_{(Cu2-Cu2)}$ remarkably decreases (Fig. S2c). On the other hand, in contrast to ref. 15, B_{iso}(S2) (Fig. S2b) and $d_{(Cu2-S2)}$ (Fig. S2d) refined in this work remain nearly temperature-independent. Similar trends were observed in $Cu_{11.5}Ni_{0.5}Sb_4S_{13}$ (Fig. S1a–e). Importantly, we confirm the same tendencies also in $Cu_{12-x}Ni_xSb_4S_{13}$ (x = 0.05 and 0.2) for T > 80 K.

As mentioned above, tetrahedrites with a lower Ni-content (x = 0.05, x = 0.2) undergo the cubic ↔ tetragonal ($I\bar{4}3m$ → $P\bar{4}c2$, $a_{tetr} \approx a_{cub}\sqrt{2}$, $c_{tetr} \approx a_{cub}$) SPT below 80 K. This became clearly visible in the HR PXRD patterns, where (00l), (0kl) and some other reflections split and numerous additional peaks appear (Fig. 1a, b and 2). The structural model for this low-temperature phase is reported in ref. 17. The crystallographic data and the parameters obtained from Rietveld refinements for $Cu_{12-x}Ni_xSb_4S_{13}$ (x = 0.05, 0.2) at different temperatures based on the model of Long *et al.*[17] are collected in Tables S2 and S4. The low values of the reliability factors (R_I < 6% and R_P < 8%) for the structures in the T-range 10–70 K confirm correctness of the performed refinements.

Rather less pronounced splitting of selected (00l) and (0kl) reflections (some of them are shown in the middle panels of the Fig. 2) as well as weakening of intensities of *e.g.* (052)- and (014)-peaks in the PXRD pattern of $Cu_{11.95}Ni_{0.05}Sb_4S_{13}$ measured at T = 80 K did not allow us to well refine its structure assuming tetragonal arrangement: R_I = 8.3% and rather poor description of the profile (Fig. 2) were observed. This finding is considered as being an indication of the presence of both cubic (SG $I\bar{4}3m$) and tetragonal (SG $P\bar{4}c2$) phases in the studied sample at the mentioned temperature. Such a scenario of SPT is assumed for undoped tetrahedrite in ref. 17 as well as suggested for In_2S_3[63] and In_2Te_3.[64] And indeed, two-phase refinement converged with lower R_I^{tetr} = 7.3% (52.8 wt%) and R_I^{cub} = 4.3% (47.2 wt%) as well as much better described profile (Fig. 2). However, to confirm a two-phase character of the $Cu_{11.95}Ni_{0.05}Sb_4S_{13}$ sample at T = 80 K finally and unambiguously, an *in situ* transmission electron microscopy study, which is able to resolve micro domains of both structural modifications, would be strongly desired.

Temperature evolution of the unit cell volume (UCV) of $Cu_{11.95}Ni_{0.05}Sb_4S_{13}$ is presented in Fig. S3. As expected, UCV of its cubic modification decreases with T-decreasing down to 100 K, then suddenly increases at SPT and once the tetragonal structure is stabilized it decreases again upon further cooling. All these features are reported for undoped tetrahedrites and interestingly, they occur independently of the observed structural changes (*i.e.*, the structure remains cubic in the entire temperature range[15] or becomes tetragonal below T_{SPT}[17]).

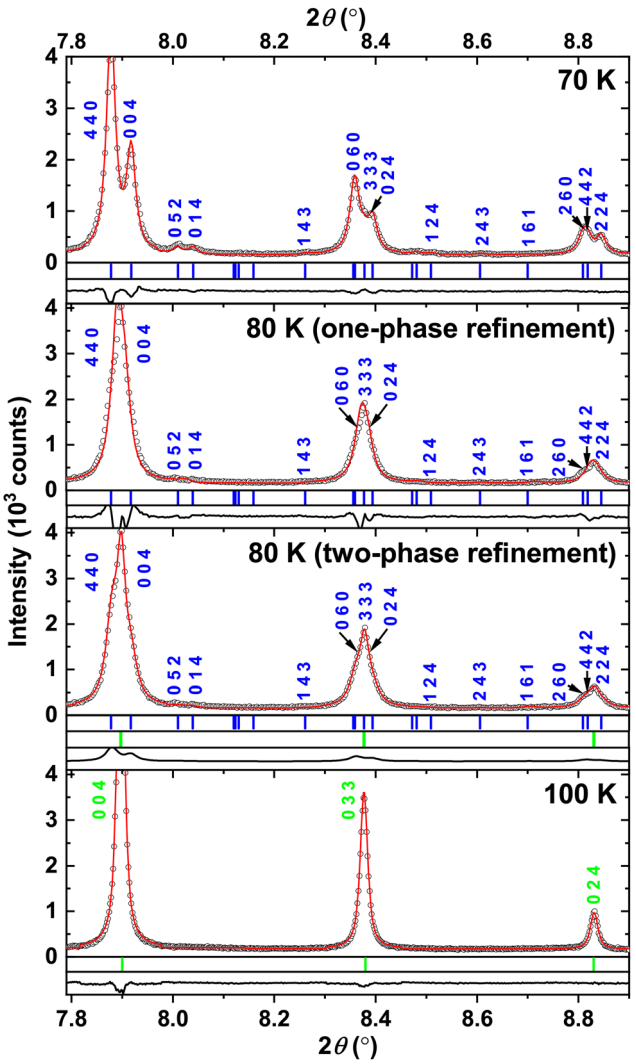

Fig. 2 Selected ranges of high resolution powder X-ray diffraction patterns of the $Cu_{11.95}Ni_{0.05}Sb_4S_{13}$ tetrahedrite measured at different temperatures together with indexing and refined profiles. Indexes of tetragonal structure are given in blue color, whereas those of the cubic one – in green.

The negative thermal expansion of $\Delta V \approx -0.25\%$ (inset to Fig. S3) in $Cu_{11.95}Ni_{0.05}Sb_4S_{13}$ at SPT is not as drastic as in TiGePt ($\Delta V \approx -10\%$)[66] or in $Zn_2P_2O_7$ ($\Delta V \approx -2\%$);[67] however, it is by a factor of $\approx$2 stronger than in stoichiometric $Cu_{12}Sb_4S_{13}$ without- ($\Delta V \approx -0.15\%$)[15] and with ($\Delta V \approx -0.11\%$)[17] cubic $\leftrightarrow$ tetragonal SPT. Such a strong ΔV-jump in $Cu_{11.95}Ni_{0.05}Sb_4S_{13}$ would suggest the structural phase transition in this compound to be of the 1st order.[2]

Interestingly, in contrast to the ternary $Cu_{12}Sb_4S_{13}$ compound, in the doped one ($x = 0.05$), a_{tetr} increases with increasing temperature, revealing a clear tendency to a saturation near T_{SPT}, whereas c_{tetr} decreases, passes through a minimum at $T_{min} \approx 50$ K and then slightly increases (Fig. S4). This results in a maximum at the same temperature in the c/a-ratio (inset to Fig. S4) as well as into a less pronounced minimum in $V(T)$-dependence (inset to Fig. S3). These structural changes are obviously responsible for a kink in the temperature dependence of magnetic susceptibility of $Cu_{11.95}Ni_{0.05}Sb_4S_{13}$ (see discussion below).

Interatomic distances (d) for tetragonal $Cu_{12-x}Ni_xSb_4S_{13}$ ($x = 0.05$ and 0.2) refined at different temperatures are collected in Table S5. To get an idea about their evolution, we compared them with those from the cubic structure based on the group–subgroup scheme, revealing corresponding relations (Fig. S5). For instance, contact Cu2–Sb (Fig. S2e) in the cubic arrangement of $Cu_{12}Sb_4S_{13}$ vary in the range of $\approx$3.29–3.09 Å (*cf.* Table S3; *i.e.*, decrease abruptly with decreasing temperature). The analogous Cu(6-7), and Cu(9-10)–Sb(1-2) distances in the tetragonal modification of $Cu_{11.95}Ni_{0.05}Sb_4S_{13}$ are $\approx$3.58–3.29 Å and remain almost temperature-independent for 10 K $< T <$ 70 K. As an example, T-evolutions of $d_{(Cu6–Sb1)}$ and $d_{(Cu10–Sb1)}$ are shown in Fig. S2e. Hence, one can conclude that if in the cubic structure the maximal change Δd_{max} for Cu2–Sb before and after SPT is of $\approx$0.2 Å, then for one of the corresponding contacts derived from it in the tetragonal structure (*i.e.*, Cu7–Sb2), it is of $\approx$0.5 Å (Tables S3 and S5). In the case of Cu–S contacts, the situation is more complex. The derived tetragonal contacts: (i) follow the cubic trend (*i.e.*, increase with temperature), as *e.g.* Cu9–S7 and Cu10–S3 (Fig. S2d), (ii) are nearly T-independent, as Cu6–S6 and Cu7–S5 (Fig. S2f) or (iii) decrease with T (Fig. S2f). And again we observe, $\Delta d_{max} \approx 0.04$ Å and $\approx$0.1 Å for cubic and tetragonal (in case of Cu9–S4 contact) modifications, respectively.

The refined ADPs of the tetragonal $Cu_{11.95}Ni_{0.05}Sb_4S_{13}$ phase are nearly temperature-independent (Table S4 and inset to Fig. 1a). Only B_{iso} of the Cu6-atom reveals a well pronounced linear increase with increasing T. As it is known, such a behavior is a signature of a possible 'rattling' effect, which is widely discussed in tetrahedrites.[19,62,68] It is ascribed to the Cu2-atoms in the 12*e*-site, which center $[S_3]$-triangles. Importantly, Cu6 (occupies 4*e*-position) is one of the atoms derived by a group–subgroup transformation from Cu2 (Fig. S5 and explanations to it below). It should be also noted that by analyzing the chemical bonding situation by calculating electron localization function (ELF) maps, the authors of ref. 17 concluded that in the ternary $Cu_{12}Sb_4S_{13}$ below T_{SPT}, Cu2–Cu2 interactions are strengthened and thus, these atoms become "locked", which indicates suppression of 'rattling'. This seems to be not the case in the slightly doped sulfide, which is also evidenced by the specific heat measurements (*vide infra*). Therefore, knowing that $B_{iso}(T)$ is given for 'rattling' atoms as:

$$B_{iso} = \left(\frac{2h^2}{\pi m_j k_B \Theta_{Ej}^2}\right) T \qquad (1)$$

with h and k_B representing Planck and Boltzmann constants, respectively, m_j the reduced mass and Θ_{Ej} the Einstein temperature, we fitted $B_{iso}(T)$ to a linear $a + bT$ dependence. The slope $b = 4.9(1) \times 10^{-22}$ m^2 K^{-1} obtained from such a fit was further used to estimate the Einstein temperature $\Theta_E^{(B_{iso},Cu6)} = 31(1)$ K in fair agreement with the value deduced from specific heat.

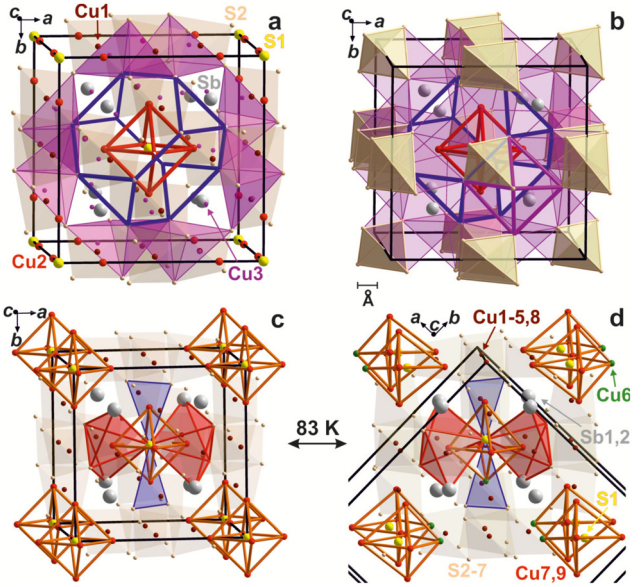

Fig. 3 (a) [S1Cu2$_6$]-octahedron (red) and [S1S2$_{12}$]-truncated tetrahedron (blue) as first- and second coordination spheres of the S1-atom together with arrangement of [Cu1S2$_4$]-tetrahedra (tan) and [Cu3S2$_5$]-tetragonal pyramids in the structure of $Cu_{13.68}Sb_4S_{13}$.[65] (b) Arrangement of empty [@S2$_4$]-tetrahedra and [@S2$_5$]-tetragonal pyramids in the same structure. (c) [S1Cu2$_6$]-octahedra (orange), [Cu1S2$_4$]-tetrahedra (tan), [Cu2S2$_3$]-triangles (blue) and [Cu2S2$_3$Sb$_2$]-trigonal bipyramids (red) in the structure of the stoichiometric $Cu_{12}Sb_4S_{13}$ tetrahedrite (Tables S1 and S2). (d) Distorted [S1Cu$_6$]-octahedra (orange), [CuS$_4$]-tetrahedra (tan), [CuS$_3$]-triangles (blue) and [CuS$_3$Sb$_2$]-trigonal bipyramids (red) in the structure of the doped $Cu_{11.95}Ni_{0.05}Sb_4S_{13}$ (Tables S3 and S4).

The standard structural arrangement of the mineral tetrahedrite has been known since 1964 and includes two sites occupied by Cu1- (12*d*) and Cu2-atoms (12*e*), and two further sites by S1- (2*a*) and S2-atoms [24*g* at ($\approx$0.11, *x*, $\approx$0.36)], whereas Sb-atoms are at the 8*c* Wyckoff position.[14] Such a crystal structure can be understood as a corner sharing array of the [Cu1S2$_4$]-tetrahedra where in the free space in-between are embedded [S1Cu2$_6$]-octahedra (Fig. 3) as well as the [SbS2$_9$]-triangular cupolas (polyhedra with hexagonal bases and triangular tops) (not shown in Fig. 3). The latter, being enlarged (*i.e.*, six Sb–S contacts are $>$4 Å), together with the free space between the first- and second coordination spheres of the S1-atom (*i.e.*, [S1Cu2$_6$]-octahedron and [S1S2$_6$]-truncated tetrahedron marked in Fig. 3a and b by red and blue colors, respectively) already indicate a lower packing density in the tetrahedrite. Additionally, this structural arrangement is characterized by empty tetrahedra and tetragonal pyramids with the centers at 6*b* (0,1/2,1/2) (tan in Fig. 3b) and at 24*g* ($\approx$0.87, *x*, $\approx$0.57) (pink in Fig. 3a and b), respectively. In some studies,[62,65] possible partial centering ($<$15%) of the triangular faces of such pyramids and thus, the $Cu_{12+y}Sb_4S_{13}$ composition, is reported. One of these variants is depicted in Fig. 3a. This low packing density in tetrahedrite is one of the important reasons for a complex phonon spectrum with pronounced 'rattling' effects.

Structural arrangement of the LT tetragonal modification of $Cu_{11.95}Ni_{0.05}Sb_4S_{13}$ (Tables S3 and S4) is presented in Fig. 3d. It is characterized by the same structural units as those of the HT modification, which however, reveal different levels of distortion. The latter are most pronounced in the case of [SCu$_6$]-octahedra. Interestingly, despite the slight corrugation of the triangular base (blue in Fig. 3c and d) of the [CuS$_3$Sb$_2$]-trigonal bipyramid (red in Fig. 3c and d) in the tetragonal structure, the Cu-atoms remain in their centers.

The structural relationships between LT- and idealized (no split- and partially occupied positions) HT-$Cu_{12}Sb_4S_{13}$ can be described on the basis of group–subgroup schemes.[69,70] The symmetry transformations within it are performed by *klassengleiche* (*k*) or *translationengleiche* (*t*) reductions (possible indexes here are 2, 3 or 4) indicating changes of the unit cell parameters or elimination of some symmetry operations. As one can see from Fig. S5, the tetragonal LT-modification can be deduced from the HT-one in three steps by performing *t*2, *t*3 and *k*2 operations. Such close structural relationships are reflected in the similarities in diffraction patterns as well as arrangements of polyhedra discussed above. Importantly, the scheme in Fig. S5 explains why only one of the twelve Cu-atoms available is responsible for possible 'rattling' (see discussion in the chapter on specific heat).

In the subsequent discussion, we will refer to the intricate changes in the crystal structure of undoped and doped $Cu_{12}Sb_4S_{13}$ as a structural phase transition (SPT).

3.2 Raman spectroscopy

Raman spectra of the ternary $Cu_{12}Sb_4S_{13}$ tetrahedrite are known to reveal four main features: (i) lattice vibrations (typical region $<$100–120 cm^{-1}) due to collective motion of whole polyhedra of heavy (Cu,Sb)-atoms relative to each other; (ii) antisymmetric bending modes ($\sim$150–250 cm^{-1}) due to bending vibrations of S–Sb–S angles where the two Sb–S bonds bend out of phase with each other; (iii) symmetric bending modes ($\sim$250–320 cm^{-1}) due to bending vibrations where Sb–S bonds bend in phase; (iv) antisymmetric stretching modes ($\sim$330–380 cm^{-1}) due to stretching of the Sb–S bond, when they elongate and contract out of phase.[39,71–76]

The deconvoluted Raman spectra of the $Cu_{12-x}Ni_xSb_4S_{13}$ tetrahedrites measured at room temperature in the 275–385 cm^{-1} range are depicted in Fig. 4. Their peak positions together with full-width at half maxima (FWHM) are collected in Table 1. The undoped ternary compound is characterized by five dominant vibrational modes, which are assigned to symmetric bending (ν_1–ν_3) and antisymmetric stretching modes (ν_4, ν_5). The overall quality of the spectra as well as four main characteristic Raman modes (the low lying ν_1 feature is frequently not resolved in the literature as well) agree well with the data reported in ref. 75, 77 and 78. Notably, no additional vibrational modes appear across the investigated doping range, suggesting the absence of secondary phases and affirming the single-phase Ni-substituted tetrahedrites.

As it is known, in accordance with the harmonic oscillator model and Hooke's law, the vibrational modes are expected to be shifted to higher wavenumbers with shortening of the bond length (*i.e.*, strengthening of chemical bonds). On the other

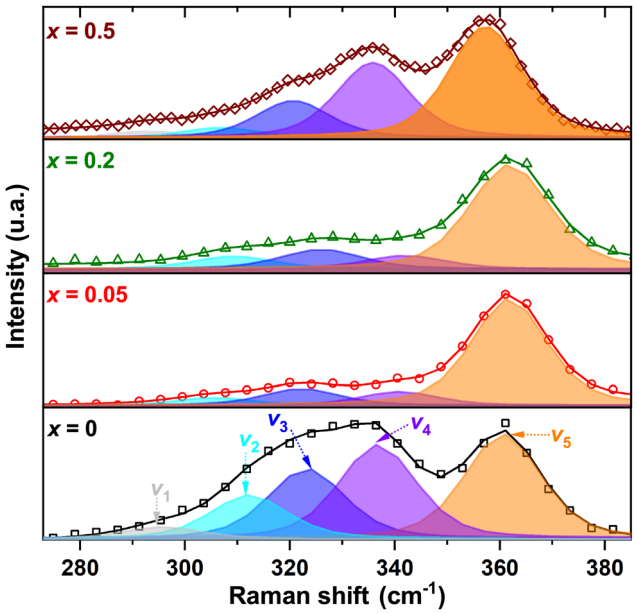

Fig. 4 Raman spectra of $Cu_{12-x}Ni_xSb_4S_{13}$ at room temperature together with the fits to Lorentzian functions allowing deconvolution of the overlapping peaks.

Table 1 Raman spectra peak positions and their full-width at the half maximum [ν(FWHM)] (both are given in cm^{-1}) in $Cu_{12-x}Ni_xSb_4S_{13}$

Ni-content	ν_1	ν_2	ν_3	ν_4	ν_5
x = 0	296(17)	312(17)	323(17)	336(17)	361(17)
x = 0.05	—	305(17)	322(17)	341(17)	362(17)
x = 0.2	—	309(18)	326(18)	342(18)	362(18)
x = 0.5	293(17)	307(17)	321(17)	336(17)	357(17)

hand, analysis of the correlations between the absolute intensities of the peaks is hampered by the rather arbitrary units of Raman scattering intensity.[72] In this respect, tracking the influence of the Cu by Ni replacement (elements, which are neighbors in periodic table and thus reveal close atomic radii and electronegativities) on the Sb–S interactions in $Cu_{12-x}Ni_xSb_4S_{13}$ is not an easy task. For instance, drastic changes (7 and 5 cm^{-1}) in the positions of ν_2 and ν_4 modes while going from x = 0 to x = 0.05 (Table 1) should be rather ascribed to the inaccuracy of the performed fits, which is caused by low spectral resolution as well as huge intensity reduction. However, evolution of the shifts of ν_4 and ν_5 modes with increasing x to a certain extent mimics the dependence of UCP on x (red points in the inset to Fig. 1b).

No drastic changes in FWHM of the observed peaks (Table 1) reflect a growing degree of lattice distortion as a result of Cu-to-Ni substitution.

3.3 Magnetic susceptibility

The temperature dependencies of reciprocal magnetic susceptibility, $\chi^{-1}(T)$, for $Cu_{12-x}Ni_xSb_4S_{13}$ are depicted in Fig. 5. For compounds with Ni-content $x < 0.5$, they decrease non-linearly down to ≈90 K and then drastically increase due to the SPT at T_K^{χ}. In contrast, $\chi^{-1}(T)$ of Ni-rich $Cu_{11.5}Ni_{0.5}Sb_4S_{13}$ is linear for 90–300 K. Reciprocal susceptibilities also clearly decrease (effective magnetic moment μ_{eff} increases) with increasing x. Furthermore, visual analysis of Fig. 5 would suggest that the absolute values of Weiss temperatures, $|\theta_W|$, become smaller for larger x. Following this observation and to obtain an idea about the behavior of magnetic Ni^{2+}-ions in $Cu_{12-x}Ni_xSb_4S_{13}$, we considered the T-ranges in which $\chi^{-1}(T)$ is linear. As one can see from Table 2, they are different for diverse x, which indicates our further analysis to be rather qualitative in nature, whereas more robust quantitative results could be obtained by extending the fitting range to 500–600 K. The results of our linear fits to a Curie–Weiss law given as $\chi = C/(T - \theta_W)$ are collected in Table 2.

The non-zero C-value is in contrast to the presumed non-magnetic nature of pristine tetrahedrite. However, the crystal structure of ternary $Cu_{12}Sb_4S_{13}$ refined in this work assumes two non-equivalent Cu-positions (*i.e.*, 12*d* and 12*e*, Table S3) and thus, even suggesting only one of them to be magnetic (*i.e.*, due to Cu^{2+}-ions with theoretically calculated effective magnetic moment $\mu_{eff}^{theor} = 3.55\mu_B$) we calculate $\mu_{eff} = 0.78(2)\mu_B$, which would indicate ≈5% of Cu^{2+}-impurities (a number which is in good agreement with that deduced from X-ray absorption spectra measured for undoped tetrahedrite at $CuL_{II,III}$ edges[79]) in the studied compound. This observation together with the predominantly non-linear behavior of $\chi^{-1}(T)$ and large $|\theta_W|$-value would rather imply that the T-dependence of the susceptibility is due to impurities, whereas that of an ideal $Cu_{12}Sb_4S_{13}$ should be similar to a Pauli paramagnetic metal (*i.e.*, small and nearly constant).

As one can see from Table 2, Ni-doping expectedly increases C. However, calculation of the effective moment for the sample with x = 0.05, assuming the C-parameter to be only due to Ni^{2+}, results in a value inconsistent with the chemical composition of the sample. Subtraction of the Cu^{2+}-impurity contribution in this case

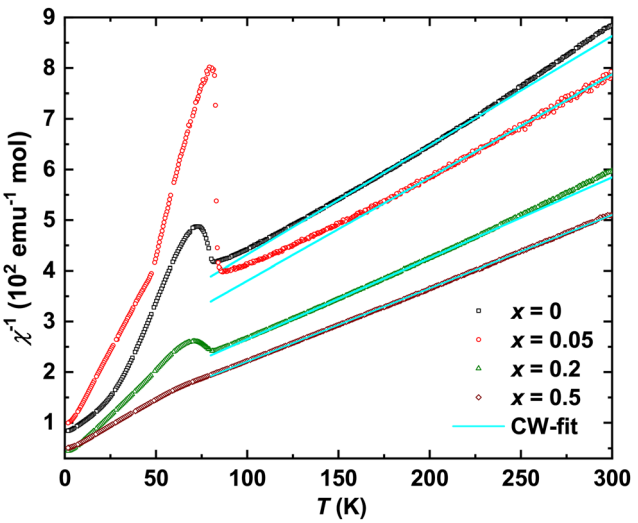

Fig. 5 Temperature dependence of reciprocal magnetic susceptibility $\chi^{-1}(T)$ ($\mu_0 H$ = 7 T) for $Cu_{12-x}Ni_xSb_4S_{13}$ together with the fits to Curie–Weiss law.

Table 2 Parameters of $Cu_{12-x}Ni_xSb_4S_{13}$ deduced from magnetic susceptibility, fit to the Curie–Weiss law as well as theoretical calculations

Parameter	x = 0	x = 0.05	x = 0.2	x = 0.5
Magnetic susceptibility				
T-range of fit, K	155–255	200–300	125–225	125–300
C, emu K mol^{-1}	0.464(9)	0.491(9)	0.626(9)	0.692(9)
μ_{eff}/Ni-at., μ_B	—	—	5.00(2)	3.32(2)
θ_W, K	−100.4(9)	−86.7(9)	−66.0(9)	−52.9(9)
T_k^{χ}, K	78(1)	83(1)	76(1)	71(2)
$\lvert\Delta\chi_0\rvert$, 10^{-9} m^3 mol^{-1}	4.57(8)	15.71(8)	2.39(7)	—
$\Delta\gamma_0$, mJ mol^{-1} K^{-2}	26.5(5)	91.1(5)	13.9(4)	—
$\Delta N_{\chi}^{(E_F)}$, st. eV^{-1} f.u.$^{-1}$	11.3(2)	38.7(2)	5.9(2)	—
ΔT_{max}, K	1.9(1)	7.1(1)	2.1(1)	—
Rigid-band approximation (RBA)				
$N_{cub}^{(E_F)}$, st. eV^{-1} f.u.$^{-1}$	20.2(1)	20.6(1)	20.5(1)	22.2(1)
$N_{tetr}^{(E_F)}$, st. eV^{-1} f.u.$^{-1}$	10.8(1)	10.8(1)	15.0(1)	21.7(1)
$\Delta N_{RBA}^{(E_F)}$, st. eV^{-1} f.u.$^{-1}$	9.4(1)	9.8(1)	5.5(1)	0.5(1)
Virtual crystal approximation (VCA)				
$N_{cub}^{(E_F)}$, st. eV^{-1} f.u.$^{-1}$	—	20.3(1)	20.5(1)	22.6(1)
$N_{tetr}^{(E_F)}$, st. eV^{-1} f.u.$^{-1}$	—	5.5(1)	21.6(1)	29.3(1)
$\Delta N_{VCA}^{(E_F)}$, st. eV^{-1} f.u.$^{-1}$	—	14.8(1)	−1.1(1)	−6.7(1)

is rather impossible. On the other hand, μ_{eff} for $Cu_{12-x}Ni_xSb_4S_{13}$ with x = 0.2 and 0.5 already agrees with the effective magnetic moment expected for Ni^{2+}-ions ($\mu_{eff}^{theor} = 5.59\mu_B$ and $\mu_{eff}^{exp} = 3.2\mu_B$).[2]

The SPT at a critical temperature T_k^{χ} manifests itself in $\chi^{-1}(T)$ of the studied tetrahedrites by a jump, $\lvert\Delta\chi_0\rvert$ (Fig. 5). T_k^{χ} slightly increases in lightly doped $Cu_{11.95}Ni_{0.05}Sb_4S_{13}$ and then decreases with increasing x (Table 2). The drastic structural change, when the crystal structure changes its symmetry to tetragonal, for the compound with x = 0.05, is reflected in the sharpest and strongest $\lvert\Delta\chi_0\rvert$ jump. Furthermore, in contrast to other members of the solid solution, $\chi^{-1}(T)$ of $Cu_{11.95}Ni_{0.05}Sb_4S_{13}$ shows an additional kink at $T_k^{\chi(2)}$ = 49 K, which coincides with the minimum observed in its temperature dependencies of the UCPs of the tetragonal structure (Fig. S4). Interestingly, despite the same type of transition as well as a similar structural phenomenology (Tables S3 and S4, Fig. S2), $\lvert\Delta\chi_0\rvert$ at T_k^{χ} for $Cu_{11.8}Ni_{0.2}Sb_4S_{13}$ is even smaller than that for the undoped tetrahedrite characterized by just an enhancement of structural disorder. The transition in the compound with higher Ni-content (x = 0.5) is almost completely smoothed out (Fig. 5), which makes the estimation of $\lvert\Delta\chi_0\rvert$ impossible (Table 2).

Since both Pauli susceptibility and electronic specific heat are proportional to the density of states (EDOS) at the Fermi level (E_F), they can be used to estimate the reduction of EDOS corresponding to a gap opening at T_k. The values of the $\lvert\Delta\chi_0\rvert$ jumps at T_k are collected in Table 2. Assuming the Sommerfeld–Wilson ratio[80] to be equal to 1, one obtains a change in the Sommerfeld coefficient of electronic specific heat $\Delta\gamma_0 = \Delta\chi_0 R_0$, where $R_0 = \pi^2 k_B^2/3\mu_0\mu_B^2$. Furthermore, we recalculate it in an EDOS reduction $\left[\Delta N_{\chi}^{(E_F)}\right]$ at T_k. As one can see from Table 2, the latter values are by nearly one order of magnitude higher than those typically observed at charge density wave (CDW) transitions[81–83] and would rather indicate a 1st order phase transition in $Cu_{12}Sb_4S_{13}$. Furthermore, the EDOS reduction deduced from DFT calculations $\left[\Delta N_{RBA}^{(E_F)}\right]$ reveals the same trend as the values obtained from the magnetic susceptibility and the absolute jumps even match for the compound with x = 0.2. For a more detailed discussion on this topic, we refer to the section devoted to theoretical calculations.

Measuring $\chi(T)$ in cooling mode at 3.5 T down to 1.8 K, then switching the field to 7 T and further performing the measurement in a warming up regime, a clear hysteresis near T_k is observed for compounds with x = 0, 0.05 and 0.2 (Fig. S6). Its absence for x = 0.5 corroborates the thermal rather than magnetic nature of the effect, which is also confirmed for tetrahedrites with diverse compositions in the literature.[16,84] Importantly, the width of hysteresis ΔT_{max} at the transition temperature (Table 2) reveals nearly the same trend as the $\lvert\Delta\chi_0\rvert$ jump (*i.e.*, it is the largest for x = 0.05). This is because both ΔT_{max} and $\lvert\Delta\chi_0\rvert$ are dependent on the energy barrier height between the phases. An additional factor influencing ΔT_{max} is the nucleation time of the new phase. To shed light on this process, time-dependent kinetic studies would be required.

3.4 Specific heat

The temperature dependencies of the specific heat capacities for $Cu_{12-x}Ni_xSb_4S_{13}$ in $c_pT^{-3}(T)$ presentation are depicted in Fig. 6 and inset therein. The ternary compound (x = 0) besides the anomalies due to SPT at 78 K (Table 3) reveals a well pronounced hump centered at ≈4–5 K. The latter becomes stronger in the slightly doped sample (x = 0.05) and completely disappears in the specimens with higher Ni-content (x = 0.2 and x = 0.5) (inset to Fig. 6). As it is known, the low-temperature (LT) bosonic peak is frequently associated with the 'rattling' motion of the weakly bound atoms being situated in enlarged voids. It is a hallmark of the so-called cage-compounds (*e.g.* intermetallic clathrates,[3] filled skutterudites,[4] Remeika phases,[85] *etc.*), where 'rattling' also causes the appearance of low-energy

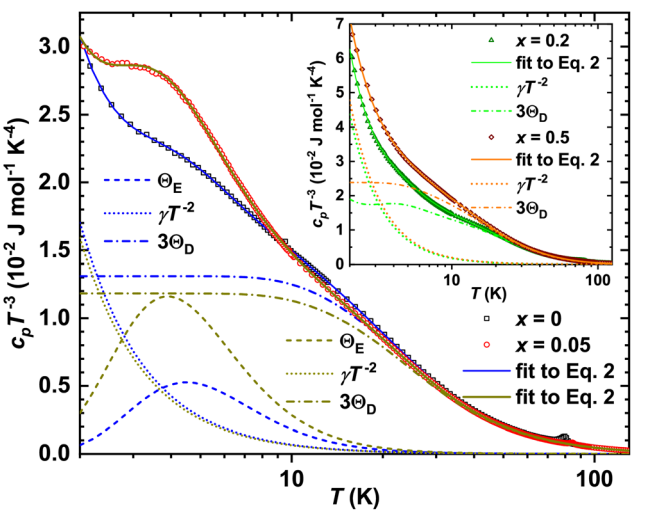

Fig. 6 Temperature dependent specific heat capacity for $Cu_{12-x}Ni_xSb_4S_{13}$ in the $c_pT^{-3}(T)$ presentation, together with the fit to eqn (2) as well as separated phononic (Θ_D, Θ_E) and electronic (γT^{-2}) contributions for x = 0, 0.05 (main panel) and x = 0.2, 0.5 (inset).

Table 3 Parameters of $Cu_{12-x}Ni_xSb_4S_{13}$ deduced from the specific heat, electrical transport properties and theoretical DFT calculations

Parameter	$x = 0$	$x = 0.05$	$x = 0.2$	$x = 0.5$
Specific heat				
$T_k^{c_p}$, K	80(1)	85(1)	83(1)	75(3)
N_{tot}	82(1)	83(1)	85(3)	57(1)
$N_D^{(1)}$	50(2)	51(5)	53(4)	44(2)
$\Theta_D^{(1)}$, K	377(9)	390(9)	404(9)	202(9)
$N_D^{(2)}$	27(1)	28(2)	31(4)	12(1)
$\Theta_D^{(2)}$, K	141(5)	141(5)	132(9)	88(3)
$N_D^{(3)}$	4.7(9)	3.3(8)	0.8(1)	0.7(1)
$\Theta_D^{(3)}$, K	79(2)	77(4)	40(1)	37(2)
N_E	0.32(7)	0.46(1)	—	—
Θ_E, K	22(1)	19(1)	—	—
γ_{DE}, mJ mol^{-1} K^{-2}	68(2)	63.6(9)	203(1)	191(1)
$\Delta S/R$ at $T_k^{c_p}$	2.7(1)	0.9(1)	4.9(1)	2.6(1)
Rigid-band approximation (RBA)				
γ_{RBA}^{cub}, mJ mol^{-1} K^{-2}	47.7(9)	48.6(9)	48.5(9)	52.3(9)
γ_{RBA}^{tetr}, mJ mol^{-1} K^{-2}	25.6(9)	25.7(9)	35.5(9)	51.1(9)
Electrical transport				
$\Delta\alpha$, μV K^{-1}	28(1)	18(1)	37(1)	—
A, 10^{-7} μV K^{-2}	2.03(1)	1.65(1)	2.56(1)	—
E_F, eV	−0.18(1)	−0.22(1)	−0.14(1)	—
2PB-formalism				
E_F^{2PB}, meV	−82	−86	−75	—
E_g^{2PB}, meV	−67	−88	−53	—
m_1/m_2	1.51	5.83	1.25	—

optical modes in the phonon spectrum. Clear LT maxima in $c_pT^{-3}(T)$ of the ternary $Cu_{12}Sb_4S_{13}$ tetrahedrite are reported in ref. 15 and 18. A 'rattling' effect in this class of compounds is also widely discussed in the literature.[18–20,28] To describe such a temperature dependence of the specific heat, the following model[86,87] is applied:

$$c_p(T) = \gamma_{DE}T + \sum_i C_D^{(i)}(T) + \sum_j C_E^{(j)}(T) \quad (2)$$

where γ_{DE} is the Sommerfeld coefficient of the electronic specific heat, and the Debye $C_D^{(i)}(T)$ and Einstein $C_E^{(j)}(T)$ terms are for the phonon spectra of the covalently bonded frameworks and of the low-energy optical modes arising from the 'rattling' motion, respectively. Hence, both these phononic contributions are dependent on the corresponding characteristic temperatures [*i.e.*, $\Theta_D^{(i)}$, $\Theta_E^{(j)}$] as well as on the numbers of modes $N_{tot} = N_D^{(i)} + N_E^{(j)}$ as follows:

$$C_D^{(i)}(T) = 3N_D^{(i)}R\left[\frac{T}{\Theta_D^{(i)}}\right]^3 \int_0^{\Theta_D^{(i)}/T} \frac{x^4e^x}{(e^x-1)^2}dx \quad (3)$$

$$C_E^{(j)}(T) = N_E^{(j)}R\left[\frac{\Theta_E^{(j)}}{T}\right]^2 \frac{e^{\Theta_E^{(j)}/T}}{\left(e^{\Theta_E^{(j)}/T}-1\right)^2} \quad (4)$$

There were few attempts to apply such a model for the description of heat capacity of undoped[18,28] as well as of doped[20,28] tetrahedrites. All of them were based on the assumption that there are three Einstein oscillators (two are associated with the motion of trigonally coordinated Cu-atoms and one is due to vibrations of Cu in 12*e*), thus indicating $j = 3$. However, none of the Einstein temperatures obtained in these studies coincided with the value of that deduced from the temperature dependence of thermal displacement parameters of Cu in 24*g*-site.[15] Therefore, based on our structural refinements, which indicated the LT bosonic peak to be a property of the tetragonal structural modification of tetrahedrite, where only Cu6 is expected to show 'rattling' motion, we propose to consider the stoichiometry as $Cu_{11}CuSb_4S_{13}$. Hence, one expects three Debye-terms with $N_D^{(i)} = 33$, 12, and 39; one Einstein-mode with $N_E = 3$ and thus in total $N_{tot} = 87$.

The results of the fit of temperature dependencies of specific heat of the studied tetrahedrites to eqn (2) are collected in Table 3. In samples with $x \leq 0.2$, the obtained N_{tot} values are in fair agreement with the theoretical expectation, whereas from $N_D^{(1)}$, $N_D^{(2)}$ and $N_D^{(3)}$ only the second one is acceptably close to the $N_D^{(i)} = 33$ expected from the vibrations of the Cu_{11}-sublattice. Importantly, $N_D^{(3)}$ became gradually smaller with increasing Ni-content x. Furthermore, an Einstein term is not needed to describe $c_p(T)$ of $Cu_{11.8}Ni_{0.2}Sb_4S_{13}$, which could indicate a simplification of the phononic spectrum with doping enhancement. This tendency is confirmed for the $x = 0.5$ compound, where a drastic reduction of the $N_D^{(2)}$-term is additionally the case. The Einstein temperatures obtained for $x = 0.05$ and $x = 0.2$ match well with $\Theta_E = 19$ K reported for undoped tetrahedrite.[15] To summarize, the strong discrepancies between predicted and experimental $N_D^{(i)}$ and N_E indicate that the phononic spectrum of tetrahedrite is far too complex to be described with a simplified Debye–Einstein model given by eqn (2). However, such a model is known to work fairly well in the case of some intermetallic clathrates[86] or filled skutterudites,[88] where 'rattling' modes can be clearly differentiated from those originating from a strongly covalently bonded framework. In contrast, $c_p(T)$ of chalcogenides containing transition metals frequently reveals significant deviations[64,89,90] from the combined Debye–Einstein theory. This can be explained by the fact that the type of chemical bonding for both 'rattling'-atoms as well as within the framework is predominantly covalent and does not differ significantly.

The Sommerfeld coefficients of the electronic specific heat deduced from the fit to eqn (2) for the studied tetrahedrites deviate strongly from the theoretically predicted values (Table 3). However, despite these differences, some trends are clearly reproduced: (i) $\gamma_{DE}^{(x=0)} > \gamma_{DE}^{(x=0.05)}$ in agreement with $\gamma_{theor}^{cub,(x=0)} > \gamma_{theor}^{tetr,(x=0.05)}$ and (ii) γ_{DE} of tetrahedrites with higher Ni-content ($x = 0.2$ and $x = 0.5$) are expectedly larger than those of undoped and slightly doped compounds. The discrepancies in absolute magnitudes as well as $\gamma_{DE}^{(x=0.2)} > \gamma_{DE}^{(x=0.5)}$ (despite the theoretical expectations) could be therefore ascribed to the presence of a minor impurity. The latter were detected by Fourier transform infrared (FTIR) absorption spectroscopy performed in our previous studies on $Cu_{12-x}Ni_xSb_4S_{13}$ tetrahedrites.[50–52] Distinct absorption peaks appearing in the mid-infrared region of 1977–2160 cm^{-1} were attributed to molecular species with B–H bonds,[91–93] which are most likely retained due to the elevated decomposition temperature

(≈800 K) of $NaBH_4$.[94] Importantly, the spectral range of 2500–3500 cm^{-1}, typically indicative of organic-based residues such as C–O, C–C–O, O–H, CH_2, and C–H related vibrations,[95,96] does not contain any detectable peaks.

Herewith, it is important to stress that $\gamma \approx 50$ mJ mol^{-1} K^{-2} (*i.e.*, which would be in excellent agreement with the theoretically obtained γ^{cub}_{theor} value) for $Cu_{12}Sb_4S_{13}$ is reported only in ref. 30, whereas other works provide much higher values of 85 mJ mol^{-1} K^{-2} (ref. 18) and even 184 mJ mol^{-1} K^{-2}.[20] Also, doping is shown to lead to an increase of the Sommerfeld coefficients of the electronic specific heat in ref. 20 and 30.

To analyze the SPT in tetrahedrites, we present their specific heat capacities as $c_pT^{-1}(T)$ in Fig. 7. It is visible that the peaks at the transitions reveal a singularity form for $x = 0$ and $x = 0.05$ samples and with further increase of Ni-content they become smeared out. Such an effect is also reported in the $Cu_{12}Sb_{4-x}As_xS_{13}$ series and is ascribed to enhancement of chemical disorder.[84] Subtracting the phononic $\left[\sum_i C_D^{(i)}(T) + \sum_j C_E^{(j)}(T)\right]$ contribution from $c_p(T)$ we obtain the electronic part (c_{el}) of the specific heat (Fig. 7). In a further step, the entropy [$\Delta S(T)$] at the phase transition was calculated by integrating the $c_{el}/T(T)$ dependence (inset in Fig. 7). It is large for all $Cu_{12-x}Ni_xSb_4S_{13}$ compounds and varies in the range of ≈1–5R in agreement with earlier reports and possible 1st order type of this phase transition.[16] The enhanced values of $\Delta S(T)$ clearly indicate that SPT is affecting the whole sample volume. Interestingly, in the $x = 0.05$ sample (*i.e.*, minor structural disorder) the cubic ↔ tetragonal transition is accompanied by a smaller entropy change compared to those in the specimens with no structural rearrangement ($x = 0$) or characterized by stronger disorder ($x = 0.2$).

3.5 Electrical transport

Temperature dependencies of electrical resistivity $\rho(T)$ for $Cu_{12-x}Ni_xSb_4S_{13}$ in comparison with selected literature data are presented in Fig. 8a. In all cases, $\rho(T)$ reveals a semiconducting type of behavior, *i.e.*, it is in the mΩ m-range as well as decreases with increasing T below SPT (Fig. 8b). Also, for our samples, $\rho(T)$ becomes larger with higher Ni-content x in the LT-range, which would agree with the enhancement of the structural disorder. However, the strongest decrease observed here for the $x = 0.2$ specimen is comparable with that reported for the ternary $Cu_{12}Sb_4S_{13}$ tetrahedrite in ref. 15. Furthermore, this effect is found to be even stronger in ref. 18. Comparing the data from ref. 15 and 18, one would also need to note that the latter reveal both more pronounced insulating and metallic behavior below and above SPT, respectively. Additionally, Rana *et al.* report on a shoulder at around 250 K (Fig. 8c), which is confirmed in ref. 17 and 97 and is shown to reveal a hysteresis in ref. 84. The latter study ascribed it to the fragility of the porous cold-pressed samples. All these as well as the fact that $\rho(T)$ is the lowest for $x = 0.05$ in the HT-regime (Fig. 8c, among specimens studied here), would be in line with pronounced sensitivity of electrical transport in semiconductors to sample's consistency, minor impurities, defects, structural imperfections, *etc.*

Since our samples were very brittle, we only succeeded in the preparation of an appropriate specimen for Hall-effect measurement from the ternary $Cu_{12}Sb_4S_{13}$ tetrahedrite ($x = 0$). The obtained temperature dependence of the Hall coefficient $R_H(T)$ is depicted in Fig. 9. It smoothly increases with increasing T, reveals a jump at SPT and then remains nearly T-independent. Since $R_H(T)$ is negative in the whole studied T-range, an electron-like conduction mechanism is expected.

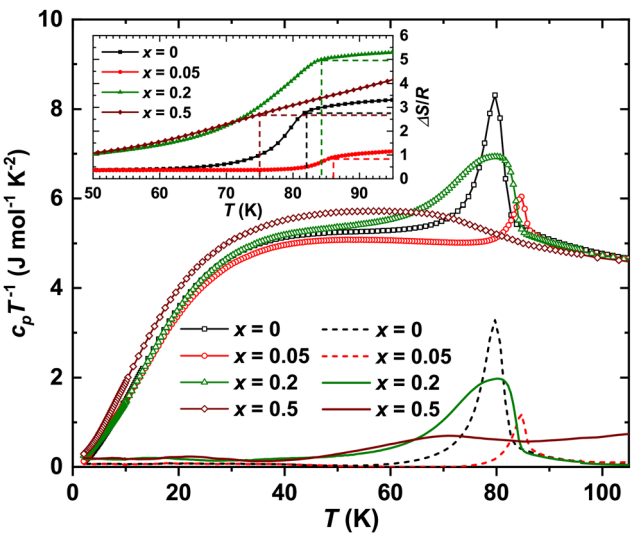

Fig. 7 Temperature dependencies of specific heat capacity (symbols with lines) and its electronic part c_{el} (lines) for $Cu_{12-x}Ni_xSb_4S_{13}$ in the $c_pT^{-1}(T)$ presentation. Inset: temperature evolution of entropy close to the structural phase transition.

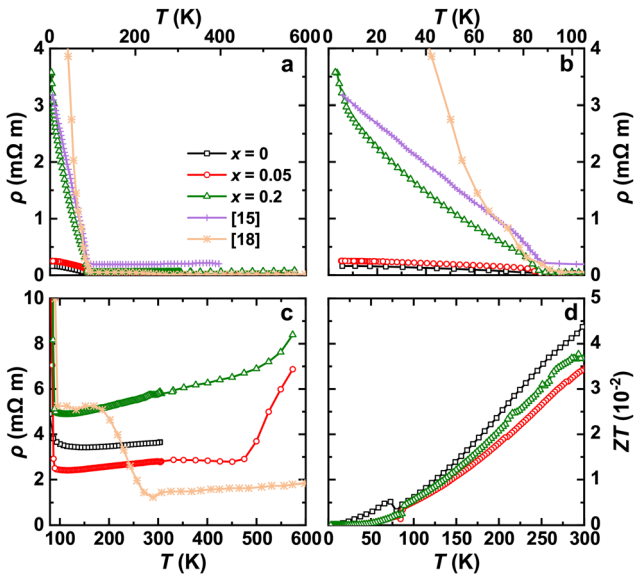

Fig. 8 (a) Temperature dependencies of electrical resistivity $\rho(T)$ for $Cu_{12-x}Ni_xSb_4S_{13}$; (b) $\rho(T)$ in the low-temperature range; (c) $\rho(T)$ in the high-temperature range; (d) temperature dependencies of thermoelectric figure-of-merit $ZT(T)$.

Employing $R_H = -(ne)^{-1}$, we calculated the temperature dependence of charge carrier concentration $n(T)$ presented in the inset to Fig. 9. It mimics $R_H(T)$ and reveals a jump near the SPT by approximately one order of magnitude. This behavior is reminiscent of that reported for $Cu_{12}Sb_4S_{13}$ in ref. 18, with the only difference in the change accompanying the phase transition, which is by a factor of $\approx 10^3$ larger (*i.e.*, from $\approx 10^{18}$ cm^{-3} to $\approx 10^{21}$ cm^{-3}) in the latter sample. The less pronounced semiconductor ↔ metal transition for our sample is already clearly reflected in the tiny jump in $\rho(T)$ (Fig. 8b). Obviously, the good electrical conductivity in $Cu_{12}Sb_4S_{13}$ studied here is mainly due to a temperature-independent metallic-like mobility of charge carriers: $\mu = |R_H/\rho| = 550(20)$ cm^2 V^{-1} s^{-1} (inset to Fig. 9).

Temperature dependencies of the Seebeck coefficient $\alpha(T)$ for $Cu_{12-x}Ni_xSb_4S_{13}$ in comparison with the data for ternary tetrahedrite from ref. 15 and 18 are shown in Fig. 10. All of them reveal the same features: (i) a well-pronounced maximum below SPT, (ii) linear increase for ≈100–350 K and (iii) slight deviations from linearity for higher temperatures. And again, our data for $x = 0.2$ shows the same transition temperature as that of the ternary tetrahedrite reported in ref. 15. However, its jump is somewhat higher (inset of Fig. 10).

Importantly, $\alpha(T)$ is positive in all cases, which suggests the hole-dominated electrical transport. This observation is opposite to the results from Hall-effect measurements. Such a situation is normally a case for multi-band systems, *e.g.* semimetals such as Bi, Sb, FeSi, *etc.* or degenerate semiconductors with both conduction and valence bands in close vicinity to the Fermi level. Hence, since the Seebeck coefficient depends on how the energy dependence of conductivity changes near E_F ($\alpha \sim d[\ln \sigma(E)]/dE$ with $\sigma = ne\mu$), holes can dominate $\alpha(T)$ due to the band curvature or scattering mechanisms, even if electrons are responsible for $R_H(T)$.[2]

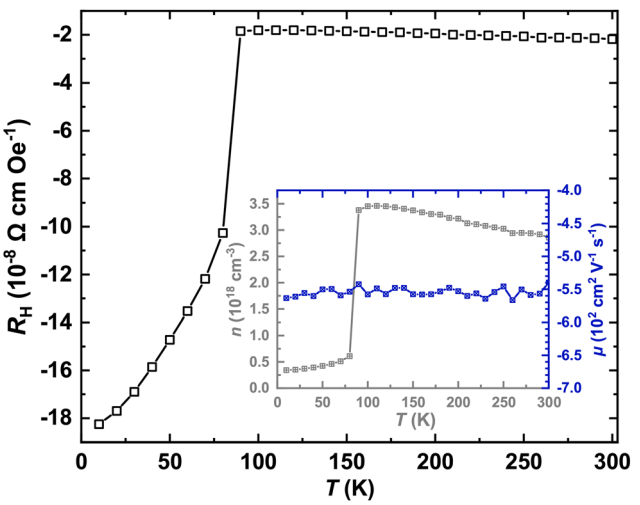

Fig. 9 Temperature dependencies of the Hall coefficient $R_H(T)$ for $Cu_{12}Sb_4S_{13}$ (the applied magnetic field was $\mu_0 H = 6$ T). Inset: temperature dependence of charge carrier concentration $n(T)$ (left gray scale) and their mobility $\mu(T)$ (right dark blue scale).

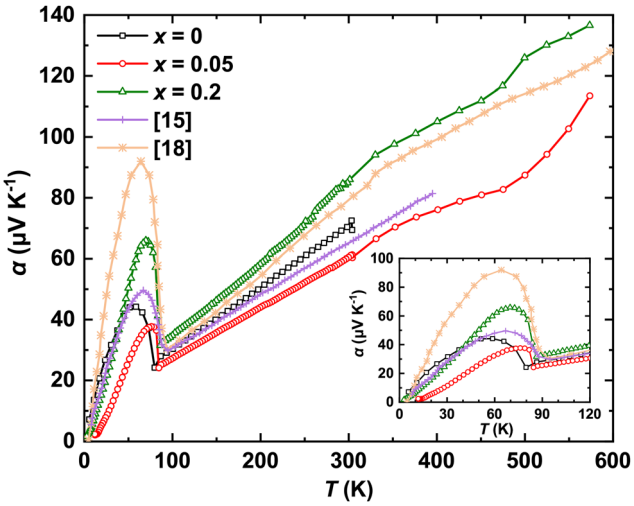

Fig. 10 Temperature dependencies of the Seebeck coefficient $\alpha(T)$ for $Cu_{12-x}Ni_xSb_4S_{13}$. Inset: $\alpha(T)$ near the structural phase transition.

Jumps $\Delta\alpha$ in the $\alpha(T)$ of $Cu_{12-x}Ni_xSb_4S_{13}$ near the SPT (inset to Fig. 10) reveal the same trend with respect to the Ni-content x as that observed for the entropy of the transition (Table 3). This finding agrees with $\alpha = q^{-1}(dS/dn)$ indicating the Seebeck coefficient to be directly related to the entropy transported per charge carrier.[2]

Finally, the linear increase of $\alpha(T)$ above SPT in the studied systems vindicates application of the Mott formula: $\alpha = AT$ with $A = (\pi^2 k_B^2/3eE_F)(r + 3/2)$, where r stands for the dominating scattering mechanism and vanishes in the case of a metal. Such a model assumes the electrical transport to occur near the Fermi energy by degenerate carriers with $k_BT \ll E_F$, which underlay elastic scattering mechanisms [*i.e.*, energy-dependent relaxation time $\tau(E)$ varies smoothly near E_F]. Importantly, it is independent of the number of bands or their dispersion shapes, thus assuming a value of Fermi energy different from the DFT calculated one.[98,99] The slopes A deduced from the linear fits of $\alpha(T)$ in the temperature range 100–300 K (not shown in Fig. 10) and E_F values calculated from them are listed in Table 3. The latter are by one order of magnitude lower than the values expected for metals or semiconductors.[2] Obviously, introducing in the Mott formula an additional scattering mechanism (ASM) ($r \neq 0$) would improve the situation; however, none of them manifest themselves in the $\mu(T)$ dependence (inset to Fig. 9).

To shed further light on the electrical transport properties in $Cu_{12-x}Ni_xSb_4S_{13}$, we analyzed $\rho(T)$ and $\alpha(T)$ above the SPT based on the Boltzmann transport formalism and two-parabolic band approximation (2PB) as implemented in the SeeBand software [see eqn (1)–(9) in ref. 100]. The corresponding fits of temperature dependencies of electrical resistivity and Seebeck coefficient suggesting 3-fold degeneracies of both bands as well as the charge carriers to be scattered on acoustic phonons and on impurities are presented in Fig. S7 and the obtained parameters are collected in Table 3.

The Fermi energies E_F^{2PB} determined from the fits are still too small; however, they are by a factor of ≈3 increased in

comparison to the values deduced from $\alpha(T)$ as well as follow their trend. The increase is obviously due to consideration of an ASM implemented in the 2PB-model, which supports the discussion above. With that, one could expect an improvement of the fits presented in Fig. S7 while increasing the number of ASM.

The sign mismatch in the Seebeck and Hall coefficients is possible if the electron mobility is larger than the hole one and hence, the relation of effective masses is expected to be as follows: $m_h^*/m_e^* > 1$. The ratios shown in Table 3 corroborate this expectation. Also, they are in fair agreement with $m_h^*/m_e^* \approx 3-8$ staying for heavy valence- and light conduction bands.[2]

In agreement with studies reporting tetrahedrites to be strongly hybridized *p*-type metallic/degenerate semiconductors (with a pseudogap and Fermi level inside the valence manifold as well as a nearly metallic electrical transport for $T > T_{SPT}$[24,30,32–38]), negative values for the energy gap E_g^{2PB} are observed (Table 3). The latter effect is difficult to explain; however, such observation is possible in the cases of a band inversion occurring in *e.g.* topological insulators[101] or of a band overlap characteristic for semimetals.[102] Obviously, tetrahedrite belongs to neither of the mentioned types of materials; however, its bands reveal a clear overlap at the Fermi level in both cubic (*e.g.* 250 and 251, 251 and 252) and tetragonal (*e.g.* 1003 and 1004) modifications (Fig. S8). Hence, the "semimetallic"-like overlap of both bands should be suggested in the 2PB-model used for the successful fitting of the experimental data. Importantly, band overlap at E_F in an electronic structure is a signature of the presence of both carrier types and thus, can give rise to sign mismatch in the Seebeck and Hall coefficients.

All these confirm again the complex character of the electrical conductivity in tetrahedrites – a system with a complex band structure near the Fermi level, which cannot be simulated by the available simplified models.

3.6 Thermal conductivity

Temperature dependencies of thermal conductivities $\kappa(T)$ for $Cu_{12-x}Ni_xSb_4S_{13}$ are depicted in Fig. 11. They are extremely low, as it is usually the case in the tetrahedrites,[15,18,38,43,62] and do not reveal a clear systematic change with increase of Ni-content x, similar to ref. 43. The minimal doping causes only a local disorder, which is insufficient to affect $\kappa(T)$ on the total scale. A similar effect is reported for $Cu_{12-x}Ni_xSb_4S_{13}$ (x = 0.1–0.4) in ref. 44.

By calculating the electronic contribution to the thermal conductivity using the Wiedemann–Franz law $[\kappa_{el} = [L(T)/\rho(T)]T$ with the temperature dependent Lorenz number $L(T) = 1.5 + \exp(-|\alpha(T)|/116)$[103]] (filled symbols in Fig. 11) we find that it is negligibly small below the SPT even for the tetrahedrites (*i.e.*, x = 0 and x = 0.05) with low $\rho(T)$ (Fig. 8b) in this temperature region. Thus, thermal transport for strongly disordered (x = 0) or tetragonal structures (x = 0.05 and x = 0.2) is dominated by phononic mechanisms ($\kappa_{ph} = \kappa_{tot} - \kappa_{el}$). This domination (>70%) remains also for $T > T_{SPT}$.

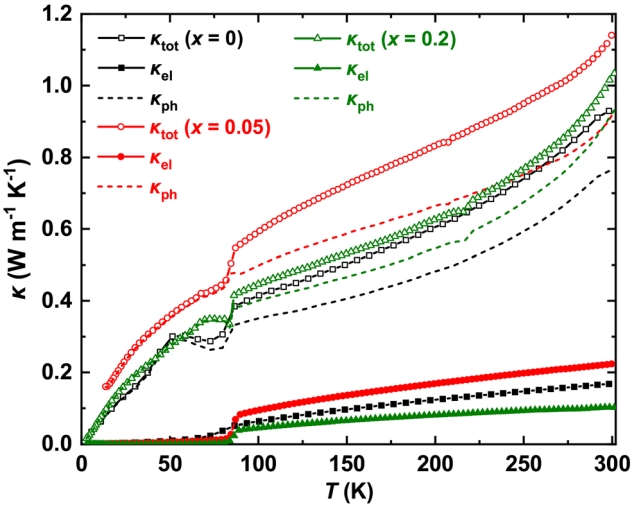

Fig. 11 Temperature dependencies of thermal conductivities $\kappa(T)$ for $Cu_{12-x}Ni_xSb_4S_{13}$ together with the electronic (κ_{el}) and phononic (κ_{ph}) contributions. Upturns in $\kappa(T)$ above 200 K are due to radiation heat losses.

To get a deeper understanding of the extremely low $\kappa(T)$ in the studied tetrahedrites, we calculated the temperature dependencies of the phonon-mean free path (l_{ph}). The latter could be obtained within the continuous and semi-classical kinetic theory from $\kappa_{ph} = (c_p v_m l_{ph})/3$,[104,105] where v_m = 1841 m s^{-1} is the velocity of sound reported for undoped $Cu_{12}Sb_4S_{13}$.[18] The $l_{ph}(T)$ values (calculated assuming the same value of v_m) for $Cu_{12-x}Ni_xSb_4S_{13}$ are depicted in the inset of Fig. 12. Expectedly, the phonon-mean free paths are by a factor of ≈2 smaller than the refined UCPs (*cf.* Table S1), which corroborates a strong scattering of phonons already within the unit cell and thus a bad thermal transport. Such an observation is known for a number of materials (*e.g.* SnSe,[106] $CaZrSe_3$,[107] $PbCuSbS_3$,[89] *etc.*) with very low $\kappa(T)$. However, here it should be stressed that the $l_{ph} < a$ finding is questionable in view of definition of the

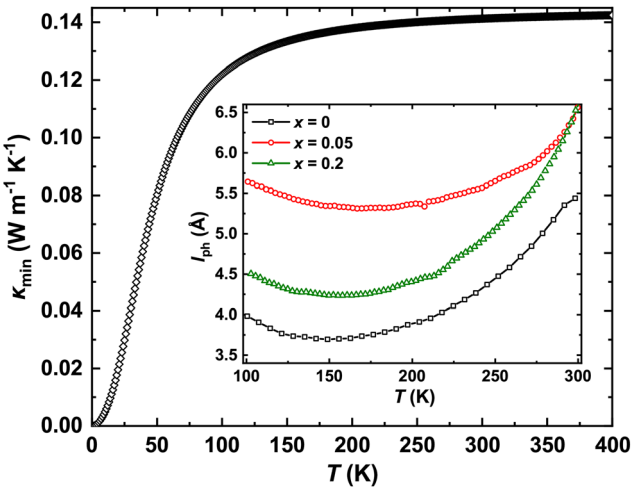

Fig. 12 Temperature dependence of minimal phononic thermal conductivity $\kappa_{min}(T)$ for $Cu_{12}Sb_4S_{13}$. Inset: temperature dependencies of the phonon-mean free path $l_{ph}(T)$ for $Cu_{12-x}Ni_xSb_4S_{13}$.

phonons, which are the excitations of the entire lattice.[2] The failure of the semi-classical kinetic theory in a precise description of extremely low thermal conductivities is, however, a widely discussed feature.[2,21]

With a complete characterization of electrical and thermal transport for $Cu_{12-x}Ni_xSb_4S_{13}$, we calculated the temperature variations of the dimensionless thermoelectric figure-of-merit defined as $ZT = \alpha^2 T/\rho\kappa$. They are presented in Fig. 8d. In agreement with earlier reports,[15,24,43] the efficiency is quite low compared to state-of-the-art materials ($ZT \geq 1$)[3] for $T < 300$ K.

One of the ways to improve the TE efficiency would be a disruption of the long-range order in tetrahedrites, *i.e.*, the achievement of an amorphous or glass-like state (importantly, the electrical transport should not be affected). In such a case, the minimal possible phononic thermal conductivity $\kappa_{min}(T)$ can be estimated from the following equation:[21,108]

$$\kappa_{min} = \left(\frac{\pi}{6}\right)^{1/3} k_B v_m N^{2/3} \left(\frac{T}{\Theta_i}\right)^2 \int_0^{\Theta_i/T} \frac{x^3 e^x}{(e^x-1)^2} dx \qquad (5)$$

with atomic density $N = 5.27 \times 10^{28}$ at. m^{-3} (calculated from UCP given in Table S1 for undoped $Cu_{12}Sb_4S_{13}$ refined at 293 K) and the $\Theta_i = v_m h(6\pi^2 N)^{1/3} k_B^{-1} \approx 201$ K Debye temperature. $\kappa_{min}(T)$ reaches its maximal value of $\approx$0.14 W m^{-1} K^{-1} for $T > 150$ K (Fig. 12) and in this temperature range is by a factor of $\approx$2–4 smaller than the experimentally observed $\kappa_{ph}(T)$ values. Obviously, such a factor of improvement of TE efficiency of $Cu_{12}Sb_4S_{13}$ in the LT-regime (*i.e.*, $T < 150$ K) will be still insufficient to reach the *ZT*-values observed in the state-of-the-art materials. Thus, to achieve a better TE performance in tetrahedrites, one must not only to transfer them into a glass-like state but also tune the electrical transport characteristics.

3.7 Electronic band structure

The calculated total (with atomic- and orbital-resolved) EDOS for the idealized (Cu in 12e without site splitting, as reported in ref. 17) cubic stoichiometric $Cu_{12}Sb_4S_{13}$ are plotted in Fig. 13a and b, respectively. As one can see, the relatively narrow ($\approx$6 eV) valence band (VB) consists of three regions: (i) a low-lying band in the form of a maximum centered at ≈ -6.1 eV due to S-3*p*, Cu1-4*s* and Cu2-3*d* states, (ii) a broad band extending from ≈ -5.8 eV to ≈ -3 eV due to hybridization of mainly S-3*p*, Cu1- and Cu2-3*d* orbitals and finally (iii) a range of ≈ -2.5 eV-E_F formed by the same states as in (ii). These bands are separated by energy gaps of $\approx$0.2 eV and $\approx$0.5 eV, respectively. There is a sizable EDOS at the Fermi level E_F (Table 2), which is dominated by the contribution of the S-3*p* orbitals. One hundred meV above the E_F is an energy gap of $\approx$1.3 eV. All these observations are in good agreement with the earlier studies.[24,30,32–38]

The EDOS of the tetragonal $Cu_{12}Sb_4S_{13}$ (for the calculation the model from ref. 17 was used) reveals almost the same features (Fig. 13c). Its main difference in comparison with that of the cubic one is the disappearance of the energy gaps in the VB as well as the narrowing of that in the conduction band to $\approx$1 eV. The character of the orbital resolved EDOS remains also almost unchanged. For better visualization we presented in Fig. 13d Cu(A)- and Cu(B)-contributions, which represent the sums of the corresponding orbitals of Cu1–Cu5, Cu8- (A) and Cu6-7, Cu9-10-atoms (B), respectively. Their relations to the Cu1- and Cu2-atoms in the cubic crystal structure are shown in the group-subgroup scheme presented in Fig. S5. As one can see from the inset to Fig. 13c and Table 2 the cubic ↔ tetragonal SPT is accompanied by a drastic reduction (*i.e.*, by a factor of $\approx$2) of EDOS at the Fermi level E_F [$N(E_F)$].

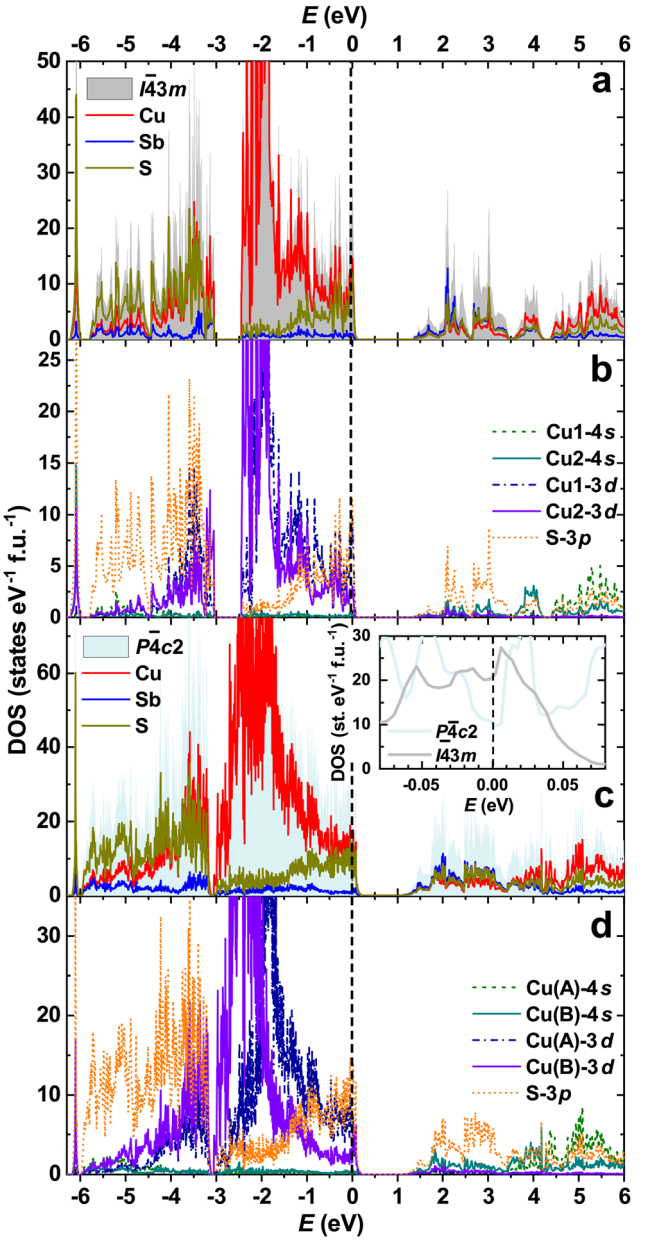

Fig. 13 Total and atomic- (a) as well as orbital-resolved (b) electronic density of states (DOS) for cubic $Cu_{12}Sb_4S_{13}$. (c) and (d) represent analogous data for the tetragonal modification, respectively. Inset to (c) contains total EDOSes for both modifications near the Fermi level (E_F).

To get an intuitive understanding of the electronic structure changes in $Cu_{12-x}Ni_xSb_4S_{13}$ upon Ni substitution we assumed the rigid-band approximation (RBA) to work. Since within this approach Ni-doping corresponds to eliminating an electron

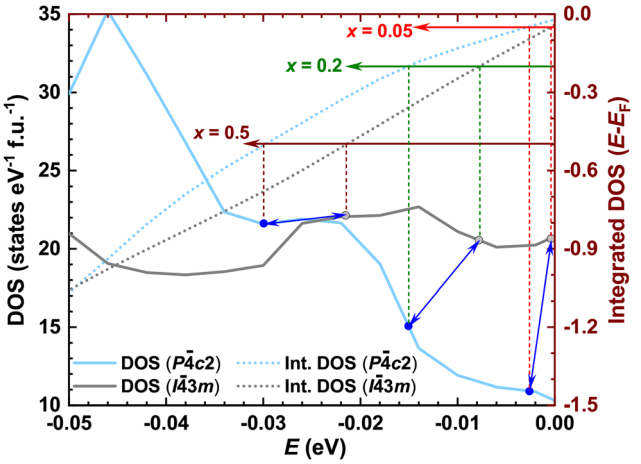

Fig. 14 Total electronic density of states (DOS) of cubic and tetragonal modifications of $Cu_{12}Sb_4S_{13}$ near the Fermi level E_F (left scale) together with the integrated DOS (right scale).

from the system, the EDOS of both tetragonal and cubic structures of ternary tetrahedrite were integrated in the energy range −0.05 eV-E_F (Fig. 14, right scales). Furthermore, projecting the corresponding electron's number (integrated EDOS) on the respective EDOS curve (Fig. 14, left scales) we were able to estimate $N(E_F)$ for different Ni-content x (Table 2). As it is clearly visible from Fig. 14, $\Delta N(E_F)$ (blue arrows) between cubic and tetragonal structures decreases with increasing x. On one hand, this change nicely explains the absence of SPT for the x = 0.5 compound; on the other it indicates that tetragonal $Cu_{12}Sb_4S_{13}$ should exist, which could not be corroborated in the current study. Obviously, despite reproducing some experimentally observed trends (see discussions above), RBA is not a perfect approach to provide complete understanding of the complex physical behaviors of the doped tetrahedrites. One of the possible reasons of this failure could be the fact that for this simulation an idealized structural arrangement was used.

Additionally, we simulate Ni-doping by applying virtual crystal approximation (VCA). The $N(E_F)$ calculated within this approach for both cubic and tetragonal modifications as well as their differences $\Delta N_{VCA}^{(E_F)}$ are collected in Table 2. As one can see, $\Delta N_{VCA}^{(E_F)}$ for x = 0.05 is now remarkably larger than that calculated from RBA, thus strengthening the conclusion about the necessity of a minor doping to trigger the cubic ↔ tetragonal SPT. However, since the $N(E_F)$ values of cubic modifications for x = 0.2 and 0.5 are larger than those of tetragonal ones, the corresponding $\Delta N_{VCA}^{(E_F)}$ are negative now. This result, however, indicates an instability of $P\bar{4}c2$-phases for both compounds, which is however in contradiction with the above discussed experimental data. Thus, similarly as RBA, also VCA can only partially explain the observed $Cu_{12-x}Ni_xSb_4S_{13}$ SPT.

4 Conclusions

Ni-doped $Cu_{12-x}Ni_xSb_4S_{13}$ (x = 0, 0.05, 0.2, 0.5) tetrahedrites were synthesized by the polyol method with further annealing and pressing of the obtained powders. The quality of the material was proved by Raman (RS) and energy dispersive X-ray (EDX) spectroscopies. They confirmed the studied specimens to be mainly single phase. None of the used spectroscopic methods were sensitive enough to confirm x = 0.05 Ni-content in the corresponding compound. However, based on the properties, this nominal composition is found to be plausible.

To shed light on the structural peculiarities in $Cu_{12-x}Ni_xSb_4S_{13}$, high resolution (HR) synchrotron powder X-ray diffraction (PXRD) characterization was performed. It revealed that in the temperature range of 100–300 K, all studied compounds crystallize with the known cubic $Cu_{12}Sb_4S_{13}$ tetrahedrite structure type [space group (SG) $I\bar{4}3m$, $a \approx 10.3$ Å], where one of the Cu-atoms is at the 24g Wyckoff position with occupancy factor G = 0.5. Since copper and nickel reveal almost identical atomic scattering factors, HR PXRD does not allow compositions' refinement. However, the latter manifests itself in the dependence of the unit cell parameters (UCPs) from Ni-content x, which is found to decrease linearly for x = 0, 0.5–2. Deviation of the UCPs of x = 0.05 and x = 0.2 from linearity can be related to the cubic ↔ tetragonal structural phase transition (SPT), which is observed for these two compositions only. The performed analysis of the interatomic distances showed complex changes. Thus, this information should be combined with analysis of the chemical bonding situation.

$Cu_{12-x}Ni_xSb_4S_{13}$ (x = 0; 0.5) revealed drastic changes in Cu2–Sb and Cu2–Cu2 contacts below 80 K; however, the crystal structure remains cubic. The cubic ↔ tetragonal SPT for x = 0.05 and 0.2 at the same temperature indicates a symmetry reduction $I\bar{4}3m \rightarrow P\bar{4}c2$ accompanied by the following changes in UCPs: $a_{tetr} \approx a_{cub}\sqrt{2}$, $c_{tetr} \approx a_{cub}$. Such a transformation is well explained within the group–subgroup scheme. A large volume (V) jump for $Cu_{11.95}Ni_{0.05}Sb_4S_{13}$ at T_{SPT} indicates the phase transition to be of 1st order. Well pronounced minima in $V(T)$- as well as $c/a(T)$-dependencies of the tetragonal structure of the x = 0.05 tetrahedrite are also reflected in magnetic susceptibility [$\chi(T)$]. Our structural study further reveals that a 'rattling' effect in the tetragonal $Cu_{11.95}Ni_{0.05}Sb_4S_{13}$ structure is due to vibrations of Cu6-atoms in the 4e position.

The temperature dependencies of reciprocal magnetic susceptibility $\chi^{-1}(T)$ for $Cu_{12-x}Ni_xSb_4S_{13}$ are almost linear for $T > T_{SPT}$ with the absolute values of χ^{-1} becoming smaller in the whole T-range with increasing x, which is in good agreement with the proposed nominal compositions. Despite estimation of the correct effective magnetic moments (μ_{eff}) in Ni-containing tetrahedrites being biased by the presence of minor Cu^{2+} contribution, their values could be obtained in the cases of x = 0.2 and x = 0.5 in good agreement with theoretical expectations for Ni^{2+}-ions. Recalculating $|\Delta\chi_0|$-jumps observed at T_{SPT} into EDOS and further comparing them with those obtained from the theoretical calculations performed within DFT we observed the same trends, thus confirming again the correctness of the proposed nominal compositions.

Bosonic peaks, indicative of 'rattling' motion, are observed for temperature dependencies of the specific heat capacities in $c_pT^{-3}(T)$ presentation for undoped ternary $Cu_{12}Sb_4S_{13}$ as well as

for slightly doped ($x = 0.05$) tetrahedrites. Considering stoichiometry of the compounds together with findings from crystal structure refinement, the combined Debye–Einstein model with three Debye- and one Einstein-term was used to describe $c_pT^{-3}(T)$. The performed fits resulted in discrepancies between theoretically expected and experimentally estimated numbers of modes, which is due to the complexity of the phononic spectra of tetrahedrites and the similarity in chemical bonding for 'rattling'-atoms and those forming the framework (*i.e.*, it is covalent in both cases). Bosonic peaks and thus, 'rattling' motion, are not observed for $Cu_{12-x}Ni_xSb_4S_{13}$ with $x = 0.2$ and 0.5. The entropy [$\Delta S(T)$] at the phase transition, deduced from the integration of the temperature dependence of electronic specific heat is large (*i.e.*, ≈ 1–$5R$) for all studied tetrahedrites, thus confirming the 1st order nature of SPT.

The electrical resistivity $\rho(T)$ of $Cu_{12-x}Ni_xSb_4S_{13}$ reveals a change from semiconducting character (decreases with increasing temperature) below SPT to a metallic one (increase with T) above SPT. Such a change is related to a drastic enhancement (*i.e.*, nearly one order of magnitude) of the charge carrier concentration. The Seebeck coefficient $\alpha(T)$ decreases nearly linearly down to T_{SPT}, which again resembles the behavior of a metallic system. However, an attempt to calculate the Fermi energy for tetrahedrites applying the Mott formula failed: the obtained E_F values were much smaller than theoretically expected ones. Jumps in $\alpha(T)$ near the phase transitions followed the trend observed in $\Delta S(T)$, which agrees with the interdependence of both quantities. Analysis of $\rho(T)$ and $\alpha(T)$ above the SPT based on the Boltzmann transport formalism and the two-parabolic bands approximation indicated that the electronic structures of studied tetrahedrites can be characterized by heavy valence- and light-conduction bands, which is in line with experimentally observed opposite signs of the Seebeck and Hall coefficients.

Thermal conductivities $\kappa(T)$ for $Cu_{12-x}Ni_xSb_4S_{13}$ are low and dominated by phononic mechanisms for $T > T_{SPT}$. Above the phase transition, the contribution of heat transport mediated by electrons reaches $\approx$30%. In line with the weak thermal transport, the phonon-mean free paths were found to be smaller than the unit cell parameters, thus indicating a failure of semi-classical kinetic theory in description of the properties of tetrahedrites. The thermoelectric efficiency of the studied compounds is poor at RT ($ZT \approx 0.03$–0.05), which is in agreement with earlier studies.

DFT calculations performed for idealized (no splits or impurity-atoms) ternary $Cu_{12}Sb_4S_{13}$ tetrahedrite revealed for both cubic and tetragonal modifications the known features of a heavily *p*-doped degenerate semiconductor: enhanced EDOS at the Fermi level E_F followed by a broad energy gap of $\approx$1 eV. In accordance with these calculations, SPT should be also accompanied by a drastic decrease of EDOS at E_F [$N(E_F)$]. Furthermore, assuming applicability of the rigid-band approximation, we deduced the changes in the EDOS $\left[\Delta N_{theor}^{(E_F)}\right]$ during the phase transitions for Ni-doped compounds. They reproduced well the trends observed in $\chi^{-1}(T)$ as well as explained the absence of SPT in tetrahedrite with $x = 0.5$ $\left[\Delta N_{theor}^{(E_F)} \approx 0\right]$. These trends were also confirmed with theoretical simulations within the virtual crystal approximation (VCA).

This study unambiguously shows that SPT in tetrahedrites is triggered by minor doping that may occur in nominally stoichiometric samples. This finding elucidates controversial reports on the symmetry lowering in the stoichiometric $Cu_{12}Sb_4S_{13}$.

Author contributions

O. B. – conceptualization, investigation, formal analysis, writing (original draft) and writing (review & editing). O. D. – conceptualization, investigation, funding acquisition, resources, writing (review & editing). V. L. – investigation, formal analysis, writing (review & editing). A. A. T. – investigation, formal analysis, writing (review & editing). R. P. – resources, investigation, writing (review & editing). A. L. J. – administration, conceptualization, writing (review & editing). R. G. – administration, conceptualization, funding acquisition, resources, writing (original draft) and writing (review & editing).

Conflicts of interest

There are no conflicts of interest to declare.

Data availability

The supplementary information contains some additional figures and tables supporting the discussions, whereas the collected and measured datasets are uploaded in OPARA. See DOI: https://doi.org/10.1039/d6tc00188b.

The experimental data that support the findings of this article are openly available,[109] embargo periods may apply.

CCDC 2516847–2516853 contain the supplementary crystallographic data for this paper.[110a–g]

Acknowledgements

This work was supported by the Ministry of Education and Science of Ukraine (0124U000541). OD thanks Alexander von Humboldt Stiftung for financial support. The DynaCool-12 system was acquired within the DFG project 422219907. The authors thank H. Borrmann for performing powder XRD and Esteban Zuñiga-Puelles for his assistance in the physical properties measurements. We also thank ESRF for providing the beamtime for this project and acknowledge technical support by Andy Fitch and Catherine Dejoie at ID22.

Notes and references

1 G. J. Snyder and E. S. Toberer, *Nat. Mater.*, 2008, **7**, 105–114.

2 R. Gross and A. Marx, *Festkörperphysik*, Oldenbourg Verlag, München, 2012.
3 *The Physics and Chemistry of Inorganic Clathrates*, ed. G. S. Nolas, Springer, Netherlands, 2014.
4 C. Uher, *Recent Trends in Thermoelectric Materials Research I*, Semiconductors and Semimetals, Elsevier, 2001, vol. 69, pp. 139–253.
5 J. He and T. M. Tritt, *Science*, 2017, **357**, eaak9997.
6 L. E. Bell, *Science*, 2008, **321**, 1457–1461.
7 G. S. Nolas, J. Sharp and J. Goldsmid, *Thermoelectrics: basic principles and new materials developments*, Springer Science & Business Media, 2001, vol. 45.
8 L. Zhao, X. Wang, F. Y. Fei, J. Wang, Z. Cheng, S. Dou, J. Wang and G. J. Snyder, *J. Mater. Chem. A*, 2015, **3**, 9432–9437.
9 W. Su, Q. Deng, L. Gan, X. Tan, Z. He, W. Yuan, C. Zhao, X. An, B. Liu and R. Ang, *Mater. Today Phys.*, 2024, **42**, 101364.
10 A. Ostovari Moghaddam, A. Shokuhfar and A. Cabot, *J. Alloys Compd.*, 2018, **750**, 1–7.
11 P. Levinský, P. K. Ventrapati, A. Dauscher, J. Hejtmánek, C. Candolfi and P. B. Lenoir, *ChemNanoMat*, 2022, **8**, e202200364.
12 D. P. Weller and D. T. Morelli, *Front. Electron. Mater.*, 2022, **2**, 913280.
13 R. Chetty, A. Bali and R. C. Mallik, *J. Mater. Chem. C*, 2015, **3**, 12364–12378.
14 B. Wuensch, *Z. Kristallogr.*, 1964, **119**, 437–453.
15 D. I. Nasonova, V. Y. Verchenko, A. A. Tsirlin and A. V. Shevelkov, *Chem. Mater.*, 2016, **28**, 6621–6627.
16 A. F. May, O. Delaire, J. L. Niedziela, E. Lara-Curzio, M. A. Susner, D. L. Abernathy, M. Kirkham and M. A. McGuire, *Phys. Rev. B*, 2016, **93**, 064104.
17 S. O. Long, A. V. Powell, S. Hull, F. Orlandi, C. C. Tang, A. R. Supka, M. Fornari and P. Vaqueiro, *Adv. Funct. Mater.*, 2020, **30**, 1909409.
18 K. S. Rana, Nidhi, C. Bera, K. Biswas and A. Soni, *J. Mater. Chem. A*, 2024, **12**, 22756–22764.
19 S. Mukherjee, D. J. Voneshen, A. Duff, P. Goddard, A. V. Powell and P. Vaqueiro, *Adv. Mater.*, 2023, **35**, 2306088.
20 E. Lara-Curzio, A. F. May, O. Delaire, M. A. McGuire, X. Lu, C.-Y. Liu, E. D. Case and D. T. Morelli, *J. Appl. Phys.*, 2014, **115**, 193515.
21 T. M. Tritt, *Thermal conductivity: theory, properties, and applications*, Springer, New York, NY, 2005.
22 R. Chetty, D. S. Prem Kumar, G. Rogl, P. Rogl, E. Bauer, H. Michor, S. Suwas, S. Puchegger, G. Giester and R. C. Mallik, *Phys. Chem. Chem. Phys.*, 2015, **17**, 1716–1727.
23 J. W. Andreasen, E. Makovicky, B. Lebech and S. K. Moller, *Phys. Chem. Miner.*, 2008, **35**, 447–454.
24 S. Tippireddy, R. Chetty, M. H. Naik, M. Jain, K. Chattopadhyay and R. C. Mallik, *J. Phys. Chem. C*, 2018, **122**, 8735–8749.
25 R. Kalbskopf, *Tschermaks Mineral. Petrogr. Mitt.*, 1972, **18**, 147–155.
26 J. Sejkora, C. Biagioni, P. Škácha, S. Musetti, A. V. Kasatkin and F. Nestola, *Eur. J. Mineral.*, 2023, **35**, 897–907.
27 C. Biagioni, J. Sejkora, S. Musetti, D. Velebil and M. Pasero, *Mineral. Mag.*, 2020, **84**, 584–592.
28 Y. Yan, N. Li, G. Wang, Q. Xiong, L. Fan, P. Jiang, X. Lu, G. Wang and X. Zhou, *Mater. Today Phys.*, 2022, **22**, 100590.
29 P. Levinsky, C. Candolfi, A. Dauscher, J. Tobola, J. Hejtmánek and B. Lenoir, *Phys. Chem. Chem. Phys.*, 2019, **21**, 4547–4555.
30 X. Lu, W. Yao, G. Wang, X. Zhou, D. Morelli, Y. Zhang, H. Chi, S. Hui and C. Uher, *J. Mater. Chem. A*, 2016, **4**, 17096–17103.
31 J. Heo, G. Laurita, S. Muir, M. A. Subramanian and D. A. Keszler, *Chem. Mater.*, 2014, **26**, 2047–2051.
32 X. Lu, D. T. Morelli, Y. Xia, F. Zhou, V. Ozolins, H. Chi, X. Zhou and C. Uher, *Adv. Energy Mater.*, 2013, **3**, 342–348.
33 X. Lu, D. T. Morelli, Y. Xia and V. Ozolins, *Chem. Mater.*, 2015, **27**, 408–413.
34 K. Knížek, P. Levinský and J. Hejtmánek, *J. Electron. Mater.*, 2019, **48**, 2018–2021.
35 C. Di Paola, F. Macheda, S. Laricchia, C. Weber and N. Bonini, *Phys. Rev. Res.*, 2020, **2**, 033055.
36 Z. Dong, T. Jiang, B. Xu, H. Zhong, B. Zhang, G. Liu, Q. Li and Y. Yang, *Miner. Eng.*, 2021, **169**, 106980.
37 K. Zazakowny, A. Kosonowski, A. Lis, O. Cherniushok, T. Parashchuk, J. Tobola and K. T. Wojciechowski, *Materials*, 2022, **15**, 849.
38 D. Moço, J. F. Malta, L. F. Santos, E. B. Lopes and A. P. Gonçalves, *Materials*, 2023, **16**, 898.
39 D. Prem Kumar, M. Ren, T. Osipowicz, R. C. Mallik and P. Malar, *Sol. Energy*, 2018, **174**, 422–430.
40 C. Xia, W. Wu, T. Yu, X. Xie, C. van Oversteeg, H. C. Gerritsen and C. de Mello Donega, *ACS Nano*, 2018, **12**, 8350–8361.
41 T. Alqahtani, M. Khan, D. Lewis, X. L. Zhong and P. O'Brien, *Sci. Rep.*, 2021, **11**, 1887.
42 Y. Liu, A. V. Kretinin, X. Liu, W. Xiao, D. J. Lewis and R. Freer, *ACS Appl. Electron. Mater.*, 2024, **6**, 2900–2908.
43 F.-H. Sun, J. Dong, S. Dey, Asfandiyar, C.-F. Wu, Y. Pan, H. Tang and J.-F. Li, *Sci. China Mater.*, 2018, **61**, 1209–1217.
44 S. Kim, G. Lee and I. Kim, *J. Electron. Mater.*, 2020, **49**, 2775–2780.
45 S. Battiston, C. Fanciulli, S. Fiameni, A. Famengo, S. Fasolin and M. Fabrizio, *J. Alloys Compd.*, 2017, **702**, 75–83.
46 T. Barbier, P. Lemoine, S. Gascoin, O. I. Lebedev, A. Kaltzoglou, P. Vaqueiro, A. V. Powell, R. I. Smith and E. Guilmeau, *J. Alloys Compd.*, 2015, **634**, 253–262.
47 M. Zubair, V. A. Lebedev, M. Mishra, T. E. Adegoke, I. S. Amiinu, Y. Zhang, A. Cabot, S. Singh and K. M. Ryan, *Chem. Mater.*, 2022, **34**, 10528–10537.
48 J. E. Daniel, C. M. Jesby, K. E. Plass and M. E. Anderson, *Chem. Mater.*, 2024, **36**, 3246–3258.
49 J. E. Daniel, S. I. Weaver, B. R. Matthias, R. Golden, G. M. George, C. Kerpal, C. L. Donley, L. E. Jarocha and M. E. Anderson, *J. Phys. Chem. C*, 2024, **128**, 13888–13899.
50 O. Dobrozhan, R. Pshenychnyi, O. Klymov, E. Zuñiga-Puelles, C. Martínez-Tomás, V. Muñoz-Sanjosé, R. Gumeniuk

and A. Opanasyuk, *Mater. Sci. Semicond. Process.*, 2024, **182**, 108690.
51 O. Dobrozhan, R. Pshenychnyi, O. Klymov, M. Yermakov, B. Boiko, S. Agouram, V. Muñoz-Sanjosé and A. Opanasyuk, *Mater. Sci. Semicond. Process.*, 2025, **194**, 109548.
52 O. Dobrozhan, R. Pshenychnyi, M. Yermakov, B. Boiko, S. Vorobiov, V. Tkáč and A. Opanasyuk, *Mater. Sci. Semicond. Process.*, 2025, **193**, 109520.
53 *STOE Powder Software, WinXPow (version 2)*, STOE and Cie GmbH, Darmstadt, 2001.
54 L. Akselrud and Y. Grin, *J. Appl. Crystallogr.*, 2014, **47**, 803–805.
55 Y. Kosaka, K. Suekuni, K. Hashikuni, Y. Bouyrie, M. Ohta and T. Takabatake, *Phys. Chem. Chem. Phys.*, 2017, **19**, 8874–8879.
56 L. Huang, Y. Wang, C. Zhu, R. Xu, J. Li, J. Zhang, D. Li, Z. Wang, L. Wang, C. Song, H. Xin, J. Zhang and X. Qin, *J. Alloys Compd.*, 2018, **769**, 478–483.
57 J. Pi, G. Lee and I. Kim, *J. Electron. Mater.*, 2020, **49**, 2710–2718.
58 N. Ghassemi, Y. Tian, X. Lu, Y. Yan, X. Zhou and J. H. J. Ross, *J. Phys. Chem. C*, 2021, **125**, 18877–18886.
59 K. Koepernik and H. Eschrig, *Phys. Rev. B*, 1999, **59**, 1743–1757.
60 J. P. Perdew and Y. Wang, *Phys. Rev. B*, 1992, **45**, 13244.
61 J. Emsley, *The Elements*, Clarendon Press, Oxford, 1998.
62 P. Vaqueiro, G. Guélou, A. Kaltzoglou, R. I. Smith, T. Barbier, E. Guilmeau and A. V. Powell, *Chem. Mater.*, 2017, **29**, 4080–4090.
63 P. Wyżga, W. Carrillo-Cabrera, L. Akselrud, I. Veremchuk, J. Wagler, C. Hennig, A. A. Tsirlin, A. Leithe-Jasper, E. Kroke and R. Gumeniuk, *Dalton Trans.*, 2020, **49**, 15903–15913.
64 E. Zuñiga-Puelles, A. Özden, R. Cardoso-Gil, C. Hennig, C. Himcinschi, J. Kortus and R. Gumeniuk, *J. Mater. Chem. A*, 2025, **13**, 9357–9371.
65 A. Lis, K. Zazakowny, O. Cherniushok, J. Tobola, M. Gajewska, T. Parashchuk and K. T. Wojciechowski, *J. Alloys Compd.*, 2024, **977**, 173337.
66 S.-V. Ackerbauer, A. Senyshyn, H. Borrmann, U. Burkhardt, A. Ormeci, H. Rosner, W. Schnelle, M. Gamża, R. Gumeniuk, R. Ramlau, E. Bischoff, J. C. Schuster, F. Weitzer, A. Leithe-Jasper, L. H. Tjeng and Y. Grin, *Chem. – Eur. J.*, 2012, **18**, 6272–6283.
67 Y. Kadowaki, R. Kasugai, Y. Yokoyama, N. Katayama, Y. Okamoto and K. Takenaka, *Appl. Phys. Lett.*, 2021, **119**, 201906.
68 Y. Xia, V. Ozoliņš and C. Wolverton, *Phys. Rev. Lett.*, 2020, **125**, 085901.
69 H. Baernighausen, *Commun. Math. Chem.*, 1980, **9**, 139–175.
70 U. Müller, *Inorganic Structural Chemistry*, Wiley, 2007.
71 B. Du, R. Zhang, K. Chen, A. Mahajan and M. J. Reece, *J. Mater. Chem. A*, 2017, **5**, 3249–3259.
72 S. Kharbish, E. Libowitzky and A. Beran, *Eur. J. Mineral.*, 2007, **19**, 567–574.
73 X. Qiu, S. Ji, C. Chen, G. Liu and C. Ye, *CrystEngComm*, 2013, **15**, 10431–10434.
74 T. Rath, A. J. MacLachlan, M. D. Brown and S. A. Haque, *J. Mater. Chem. A*, 2015, **3**, 24155–24162.
75 A. I. Apopei, G. Damian, N. Buzgar, A. Buzatu, P. Andráš and S. Milovska, *Mineral. Mag.*, 2017, **81**, 1439–1456.
76 E. Dutková, M. J. Sayagués, M. Fabián, M. Baláž, J. Kováč, J. Kováč Junior, M. Stahorský, M. Achimovičová and Z. Lukáčová Bujňáková, *Molecules*, 2023, **28**, 326.
77 U. Rout, S. Tippireddy, N. Kumari, T. Dasgupta and R. C. Mallik, *J. Appl. Phys.*, 2023, **134**, 235102.
78 U. Rout and R. C. Mallik, *Dalton Trans.*, 2024, **53**, 3511–3522.
79 R. A. D. Pattrick, G. van der Laan, D. J. Vaughan and C. M. B. Henderson, *Phys. Chem. Miner.*, 1993, **20**, 395–401.
80 M. Continentino, *Eur. Phys. J. B*, 2000, **13**, 31–35.
81 Y. Nagano, N. Araoka, A. Mitsuda, H. Yayama, H. Wada, M. Ichihara, M. Isobe and Y. Ueda, *J. Phys. Soc. Jpn.*, 2013, **82**, 064715.
82 K. Myers, S. Bud'ko, I. Fisher, Z. Islam, H. Kleinke, A. Lacerda and P. Canfield, *J. Magn. Magn. Mater.*, 1999, **205**, 27–52.
83 C. Song, J. Park, J. Koo, K.-B. Lee, J. Y. Rhee, S. L. Bud'ko, P. C. Canfield, B. N. Harmon and A. I. Goldman, *Phys. Rev. B*, 2003, **68**, 035113.
84 H. I. Tanaka, K. Suekuni, K. Umeo, T. Nagasaki, H. Sato, G. Kutluk, E. Nishibori, H. Kasai and T. Takabatake, *J. Phys. Soc. Jpn.*, 2016, **85**, 014703.
85 R. Gumeniuk, *Handbook on the Physics and Chemistry of Rare Earths*, Elsevier, 2018, vol. 54, pp. 43–143.
86 M. Beekman, W. Schnelle, H. Borrmann, M. Baitinger, Y. Grin and G. Nolas, *Phys. Rev. Lett.*, 2010, **104**, 018301.
87 Y. Ikeuchi, H. Takatsu, C. Tassel, C. M. Brown, T. Murakami, Y. Matsumoto, Y. Okamoto and H. Kageyama, *Inorg. Chem.*, 2019, **58**, 6790–6795.
88 W. Schnelle, A. Leithe-Jasper, H. Rosner, R. Cardoso-Gil, R. Gumeniuk, D. Trots, J. A. Mydosh and Y. Grin, *Phys. Rev. B*, 2008, **77**, 094421.
89 E. Zuñiga-Puelles, R. Cardoso-Gil, A. Özden, N. Bulut, V. Svitlyk, C. Himcinschi, J. Kortus and R. Gumeniuk, *Phys. Rev. B*, 2022, **106**, 195201.
90 E. Zuñiga-Puelles, A. Özden, V. Pacheco, L. Akselrud, R. Cardoso-Gil, A. Straßheim, P. Wyżga, C. Himcinschi and R. Gumeniuk, *J. Alloys Compd.*, 2024, **976**, 173055.
91 K. B. Harvey and N. R. McQuaker, *Can. J. Chem.*, 1971, **49**, 3272–3281.
92 S. Botasini and E. Méndez, *J. Power Sources*, 2012, **197**, 218–223.
93 V. D'Anna, A. Spyratou, M. Sharma and H. Hagemann, *Spectrochim. Acta, Part A*, 2014, **128**, 902–906.
94 P. Martelli, R. Caputo, A. Remhof, P. Mauron, A. Borgschulte and A. Züttel, *J. Phys. Chem. C*, 2010, **114**, 7173–7177.
95 U. V. Ghorpade, M. P. Suryawanshi, S. W. Shin, X. Wang, E. Jo, H. Bae, K. Park, J.-S. Ha, S. S. Kolekar and J. H. Kim, *J. Mater. Chem. A*, 2018, **6**, 19798–19809.

96 M. D. Regulacio, S. Y. Tee, S. H. Lim, C. P. Teng, L.-D. Koh, S. Liu and M.-Y. Han, *Nanoscale*, 2017, **9**, 17865–17876.
97 K. Suekuni, Y. Tomizawa, T. Ozaki and M. Koyano, *J. Appl. Phys.*, 2014, **115**, 143702.
98 M. Cutler and N. F. Mott, *Phys. Rev.*, 1964, **133**, A1143–A1144.
99 M. Jonson and G. D. Mahan, *Phys. Rev.*, 1980, **21**, 4223–4229.
100 M. Parzer, A. Riss, F. Garmroudi, J. de Boor, T. Mori and E. Bauer, *npj Comput. Mater.*, 2025, **11**, 171.
101 N. Orlowski, J. Augustin, Z. Gołacki, C. Janowitz and R. Manzke, *Phys. Rev. B*, 2000, **61**, R5058–R5061.
102 H. Goldsmid, *Adv. Phys.*, 1965, **14**, 273–326.
103 H.-S. Kim, Z. M. Gibbs, Y. Tang, H. Wang and G. J. Snyder, *APL Mater.*, 2015, **3**, 041506.
104 E. S. Toberer, L. L. Baranowski and C. Dames, *Annu. Rev. Mater. Res.*, 2012, **42**, 179–209.
105 O. Bourgeois, D. Tainoff, A. Tavakoli, Y. Liu, C. Blanc, M. Boukhari, A. Barski and E. Hadji, *C. R. Phys.*, 2016, **17**, 1154–1160.
106 Y. Xiao, C. Chang, Y. Pei, D. Wu, K. Peng, X. Zhou, S. Gong, J. He, Y. Zhang and Z. Zeng, *et al.*, *Phys. Rev. B*, 2016, **94**, 125203.
107 E. Osei-Agyemang, C. E. Adu and G. Balasubramanian, *npj Comput. Mater.*, 2019, **5**, 1–7.
108 D. G. Cahill and R. Pohl, *Solid State Commun.*, 1989, **70**, 927–930.
109 O. Bolielyi, O. Dobrozhan, V. Levytskyi, A. A. Tsirlin, R. Pshenychnyi, A. Leithe-Jasper and R. Gumeniuk, *Data underpinning: Controlling structural instability in the* $Cu_{12-x}Ni_xSb_4S_{13}$ (x = 0, 0.05, 0.2, 0.5) tetrahedrites, OPARA repository, Technische Universität Dresden, 2026, DOI: 10.25532/OPARA-1061.
110 (*a*) CCDC 2516847: Experimental Crystal Structure Determination, 2026, DOI: 10.25505/fiz.icsd.cc2qgzmt; (*b*) CCDC 2516848: Experimental Crystal Structure Determination, 2026, DOI: 10.25505/fiz.icsd.cc2qgznv; (*c*) CCDC 2516849: Experimental Crystal Structure Determination, 2026, DOI: 10.25505/fiz.icsd.cc2qgzpw; (*d*) CCDC 2516850: Experimental Crystal Structure Determination, 2026, DOI: 10.25505/fiz.icsd.cc2qgzqx; (*e*) CCDC 2516851: Experimental Crystal Structure Determination, 2026, DOI: 10.25505/fiz.icsd.cc2qgzry; (*f*) CCDC 2516852: Experimental Crystal Structure Determination, 2026, DOI: 10.25505/fiz.icsd.cc2qgzsz; (*g*) CCDC 2516853: Experimental Crystal Structure Determination, 2026, DOI: 10.25505/fiz.icsd.cc2qgzt0.